

TOPICAL REVIEW

## Force sensing with nanowire cantilevers

To cite this article: F R Braakman and M Poggio 2019 *Nanotechnology* **30** 332001

View the [article online](#) for updates and enhancements.



**IOP | ebooks™**

Bringing you innovative digital publishing with leading voices to create your essential collection of books in STEM research.

Start exploring the collection - download the first chapter of every title for free.

## Topical Review

# Force sensing with nanowire cantilevers

F R Braakman  and M Poggio 

University of Basel, Klingelbergstrasse 82, 4056 Basel, Switzerland

E-mail: [floris.braakman@unibas.ch](mailto:floris.braakman@unibas.ch)

Received 17 January 2019, revised 19 March 2019

Accepted for publication 16 April 2019

Published 23 May 2019



CrossMark

**Abstract**

Nanometer-scale structures with high aspect ratios such as nanowires and nanotubes combine low mechanical dissipation with high resonance frequencies, making them ideal force transducers and scanning probes in applications requiring the highest sensitivity. Such structures promise record force sensitivities combined with ease of use in scanning probe microscopes. A wide variety of possible material compositions and functionalizations is available, allowing for the sensing of various kinds of forces. In addition, nanowires possess quasi-degenerate mechanical mode doublets, which allow for sensitive vectorial force and mass detection. These developments have driven researchers to use nanowire cantilevers in various force sensing applications, which include imaging of sample surface topography, detection of optomechanical, electrical, and magnetic forces, and magnetic resonance force microscopy. In this review, we discuss the motivation behind using nanowires as force transducers, explain the methods of force sensing with nanowire cantilevers, and give an overview of the experimental progress so far and future prospects of the field.

Keywords: nanowires, nanomechanics, force microscopy, optomechanics, force sensing

(Some figures may appear in colour only in the online journal)

**1. Introduction**

Recent years have seen a dramatic reduction in the size of mechanical elements that can be used as mass and force sensors. For the most sensitive applications, micro-processed Si cantilevers are starting to give way to bottom-up fabricated structures such as nanowires (NWs) and carbon nanotubes (CNTs). Bottom-up processes rely on self-assembly or driven self-assembly and allow for the production of nanometer-scale structures with atomic-scale precision. This trend towards miniaturization is not arbitrary: smaller mechanical transducers are inherently more sensitive. At the same time, atomic-scale control in the growth of such structures presents the opportunity to drastically reduce defects, improving mechanical quality and therefore also ultimate detection sensitivity.

Among the large variety of bottom-up nanostructures, NW cantilevers are particularly promising mechanical sensors due to their high aspect ratio. A long and thin NW that is clamped on one end forms an ideal scanning probe, making it

amenable to a number of sensitive nanometer-scale imaging problems. At the same time, its symmetric cross-section results in orthogonal flexural mode doublets that are nearly degenerate. These modes allow a NW to be used as a kind of nanometer-scale force compass [1], such that both the magnitude and direction of a force can be measured. When the NW axis is oriented perpendicular to a sample surface, i.e. in the pendulum geometry, this enables the vectorial transduction of lateral forces. Moreover, the pendulum geometry allows a significant reduction of surface-induced dissipation compared to the more conventional parallel configuration. Furthermore, epitaxial growth allows the realization of NWs from a number of materials as well as heterostructures of such materials. In fact, due to their large surface-to-volume ratio, NWs are able to accommodate larger strain than conventional epitaxial films, allowing for the dislocation-free combination of materials with large lattice mismatch [2].

The application of NWs to force sensing is proving particularly apt. As highly sensitive scanning probes, NW sensors have the ability to reveal subtle force fields with high

**Table 1.** Experimentally determined parameters of singly-clamped NW cantilevers. Here the diameter  $d$  is the average cross-sectional width and  $\omega_0/2\pi$  is the average frequency of the fundamental flexural mode doublet. The quality factor  $Q$  is the average value of the fundamental flexural mode doublet, taken for a freestanding NW, far from any sample surface and measured at low ambient pressures. RT stands for room temperature.

Material	Cross-section	$d$ (nm)	$L$ ( $\mu\text{m}$ )	$\omega_0/2\pi$ (kHz)	$k$ ( $\text{N m}^{-1}$ )	$Q$	Reference
GaAs/AlGaAs	Hexagonal	350	25	417	$1 \times 10^{-2}$	50 000 (4 K)	[9, 10]
GaAs	Hexagonal	234	16.8	598	$8.3 \times 10^{-3}$	46 553 (4 K)	[11]
GaAs	Hexagonal	100	<25	1197	$8.3 \times 10^{-3}$	4900 (RT)	[12]
GaAs/AlGaAs	Hexagonal	390	20	795	$9 \times 10^{-2}$	6700 (4K)	[13]
GaAs	Hexagonal	130	14.5	465	—	2000–3000 (RT)	[14]
InAs	Hexagonal	60–80	4–5.5	2023.9	$3.6 \times 10^{-3}$	1752 (RT)	[15]
SiC	Circular	150	52	113	$4 \times 10^{-4}$	2890 (RT)	[1]
SiC	Circular	200	50	78	$1.5 \times 10^{-4}$	1000 (RT)	[16]
SiC	Circular	120	165	6.7	$3 \times 10^{-6}$	3000 (RT)	[17]
SiC	Circular	284	128	33	—	36 000 (RT)	[18]
SiC	Circular	206	93	43	—	159 000 (RT)	[18]
SiC	Circular	50	7	1519	—	2500 (RT)	[19]
SiC	Circular	300	6	6140	1.5	33 (RT, Air)	[20]
Si	Circular	44	14.4	210.5	$2.8 \times 10^{-5}$	9250 (RT)	[21]
Si	Circular	46	12.9	273	$6.6 \times 10^{-5}$	7250 (RT)	[21]
Si	—	35	15	1060	$6.5 \times 10^{-4}$	25 000 (8 K)	[6]
Si	—	50	15	333	$1.5 \times 10^{-4}$	18 000 (6 K)	[7]
Si	Circular	50	15	197.5	$2.0 \times 10^{-5}$	3000–3500 (RT)	[22]
Si	Elongated circular	60, 80	20	342	$1 \times 10^{-4}$	8150 (4K)	[8]
Si	Hexagonal	100–300	5–10	2000–6000	—	2000 (RT)	[23]
Si	Hexagonal	165	12.7	1772.4	—	3000 (RT)	[24]
Si	Hexagonal	90	9.3	2504.3	—	3000 (RT)	[24]
Si	Hexagonal	100–200	6–8	3500–4000	$2.4 - 5 \times 10^{-2}$	3000–3500 (RT)	[25]
Si	Hexagonal	150 (clamp), 60 (tip)	11.3	2480	—	—	[26]
Si	Hexagonal	39–400	2–20	1000–12 000	—	3000–25 000 (RT)	[27]
Si (metallized)	Hexagonal	142	2.25	200 000	110.3	2000 (25 K)	[28]
Si (metallized)	Hexagonal	118	2.1	188 000	62.9	2500 (25 K)	[28]
Si	Hexagonal	81	1.69	215 000	31.4	5750 (25 K)	[28]
Si	Hexagonal	74	2.77	80 000	6.0	13 100 (25 K)	[28]
CNT	Circular	50	18	270	$\sim 10^{-4}$	250 (RT)	[29]
CNT	Circular	1–3	5	38 178.5	$4.5 \times 10^{-8}$	2245 (RT)	[30]
CNT	Circular	4	1.2	5955	$2.1 \times 10^{-5}$	—	[31]
CNT	Circular	—	—	363.5	$4.8 \times 10^{-6}$	571 (RT)	[31]

spatial resolution. Unlike conventional atomic force microscopy (AFM), which reveals large, close-ranged forces—in some cases with atomic resolution—NWs are adept at discerning weak interactions. Ultra-low intrinsic mechanical losses make NWs excellent probes of tip-sample dissipation, a contrast which can be used to observe phase transitions as well as the local density of states [3–5]. The capability of nearly symmetric NWs to transduce lateral forces in two directions allows for imaging the full vectorial character of force fields. In particular, this enables the distinction of non-conservative forces, such as optical or frictional forces, from conservative ones, such as those arising from an electrical potential. Functionalized with a magnetic tip, a NW cantilever forms an excellent probe for the subtle magnetic field patterns produced by nanometer-scale magnetization textures such as domain walls, vortices, and skyrmions; superconducting vortices; mesoscopic transport in two-dimensional systems;

and small ensembles of nuclear spins. Although NW force sensors are just starting to be used for many of these applications, they have already been applied as the active sensors in some of the most sensitive and highest resolution magnetic resonance imaging experiments realized to date [6–8].

This review is structured as follows: section 2 gives an introduction to the mechanical dynamics of NW cantilevers. We first describe in section 2.1 flexural motion in a single oscillation direction and with displacement amplitudes small enough such that motion remains linear. Next, in section 2.2 we consider flexural motion in two different oscillation directions and the effects of vectorial forces and spatial force derivatives. This provides the conceptual background for the detection of 2D forces and force derivatives. We then see that shear force derivatives can lead to coupling between oscillations in two directions. As shown in section 2.3, such coupling can be used to implement coherent two-mode dynamics,

reminiscent of the dynamics of a quantum two-level system. Finally, we treat nonlinear regimes of motion in section 2.4. In section 3.1, we discuss the high force sensitivity of NW cantilevers. In particular, we cover how the geometry of a NW impacts its force sensitivity. In section 3.2, we discuss optical methods of detecting NW displacement in two directions. In section 4, we give an overview of experimental progress thus far and of the capabilities of NW transducers for specific forces. We conclude the review with an outlook for NW force transducers in section 5.

## 2. Mechanics of nanowire cantilevers

In this section, we give an overview of the mechanical behavior of NW cantilevers. Both the geometry and the material composition play an important role in determining the mechanical response of a NW cantilever to externally applied forces and force gradients, through its displacement profile, resonance frequency, and energy dissipation. NWs differ from conventional cantilevers in possessing a nearly symmetric cross-section. As we will see, this property implies that it is possible to use NW cantilevers as bidimensional force sensors. It is therefore of key importance to carefully choose the right type of NW for a specific force sensing application. Fortunately, a wide variety of NWs has become available in the last decades, produced either through bottom-up methods or by a top-down approach. This offers researchers a choice of many materials, heterostructures combining different materials, and various types of functionalization such as integrated quantum dots or magnetic tips. Furthermore, fine control over the shape of NWs has been demonstrated, yielding NWs with a tunable diameter, length, and with a variety of different cross-sections. In table 1, we list experimentally determined mechanical properties of various NW cantilevers found in literature.

In the following, we model the NW cantilever as a singly-clamped beam of length  $L$  and with a uniform cross-section along its length. Figure 1(a) schematically indicates the relevant parameters describing a singly-clamped beam undergoing flexural motion in a plane. For the purposes of force sensing, we are primarily interested in flexural modes and we do not consider longitudinal and torsional vibrations, since these modes are comparatively stiff and consequently have much higher oscillation frequencies.

### 2.1. Linear motion of a single mode

The flexural eigenfrequencies and eigenmodes of a singly-clamped beam can be derived analytically using Euler–Bernoulli theory, which gives a valid approximation when  $L$  is much larger than the cross-sectional dimension and when rotational bending and shear deformation can be neglected [32]. For a beam with a cross-section that is fully symmetric around its center (such as a cylindrical beam), the bending moment of inertia is independent of the oscillation direction. As a consequence, flexural motion takes place in an arbitrary

direction. For very asymmetric beams, such as conventional cantilever force transducers, which are flat, thin, and long, the predominant flexural motion occurs in one direction. In both cases, we can approximate the flexural motion by considering motion in one dimension. In section 2.2, we consider NWs with slightly asymmetric cross-sections, in which case we will generalize the formalism to take into account a second dimension of flexural motion.

As a starting point, we consider an idealized situation in which there is no dissipation and we do not take any driving forces into account. In this case, one can approximate the effect of a transverse force to be a torque perpendicular to both force and beam axes. An evaluation of the internal forces and torques along a flexing beam yields the following equation of motion:

$$E_Y I \frac{\partial^4 U(z, t)}{\partial z^4} + \rho A \frac{\partial^2 U(z, t)}{\partial t^2} = 0, \quad (1)$$

with  $z$  referring to the position along the beam,  $E_Y$  the Young's modulus of elasticity,  $I$  the second moment of area, which depends on the direction of flexural motion with respect to the cross-section,  $\rho$  the mass density, and  $A$  the cross-sectional area. This equation can be solved for the beam displacement  $U(z, t)$ , which can be separated into position- and time-dependent parts such that  $U(z, t) = \sum_{n=1}^{\infty} r_n u_n(z) e^{i\omega_n t}$ . Here, we sum over the  $n$  particular solutions, or modes, with  $u_n(z)$ ,  $r_n$ , and  $\omega_n$  the one-dimensional shape, amplitude, and eigenfrequency associated with the  $n$ th mode, respectively. In order for  $r_n$  to correspond to the amplitude of cantilever displacement, we use the normalization  $|u_n(L)| = 1$ . Note that this normalization entails that the  $n$  modes are orthogonal but not orthonormal.

Using the boundary conditions of a cantilever, i.e. that one end of the beam is fixed ( $u_n(0) = 0$ ) and not bending ( $u_n'(0) = 0$ ) and that the other end is free to move (zero torque:  $u_n''(L) = 0$  and zero transverse force:  $u_n'''(L) = 0$ ), for small displacements Euler–Bernoulli theory yields the mode shapes:

$$u_n(z) = C \left[ \left( \cos\left(\frac{\beta_n z}{L}\right) - \cosh\left(\frac{\beta_n z}{L}\right) \right) + \frac{\cos \beta_n + \cosh \beta_n}{\sin \beta_n + \sinh \beta_n} \left( \sinh\left(\frac{\beta_n z}{L}\right) - \sin\left(\frac{\beta_n z}{L}\right) \right) \right], \quad (2)$$

with  $C$  a normalization constant and  $\beta_n$  the dimensionless wavenumber of mode  $n$ . Figure 1(b) shows the first three of these flexural mode shapes. The modes  $u_n(z)$  can now be used in equation (1), resulting in the eigenfrequencies:

$$\omega_n = \frac{\beta_n^2}{L^2} \sqrt{\frac{E_Y I}{\rho A}}. \quad (3)$$

Table 2 lists values of  $\beta_n$  and normalized values of the eigenfrequencies.

The eigenmodes and eigenfrequencies of equations (2) and (3) correspond to the ideal case of a cantilever without dissipation and without specifying any external transverse forces. To describe realistic time-dependent behavior of the beam, we must also include dissipation and external driving forces.

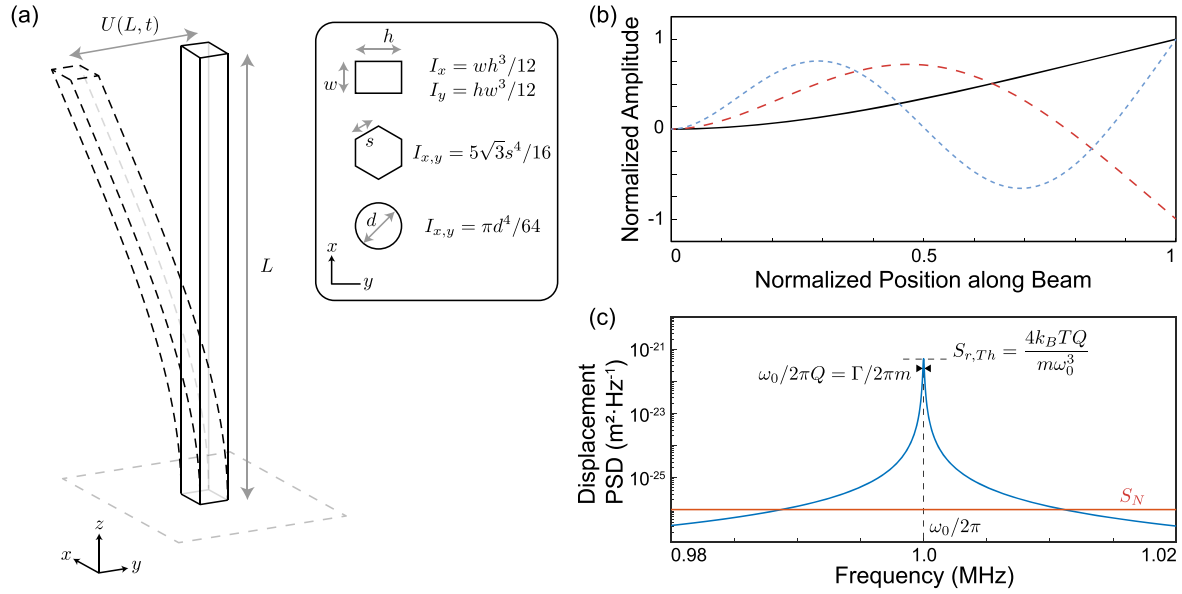


**Figure 1.** (a) Schematic overview of a singly-clamped beam. Inset shows three cross-sectional beam shapes and corresponding moments of inertia. (b) Mode shapes of the first three flexural modes of a singly-clamped beam (solid line:  $n = 0$ ; dashed line:  $n = 1$ ; dotted line:  $n = 2$ ). (c) Plot of displacement power spectral density of a thermally driven resonator, for typical values of  $Q$ ,  $\omega_0$  and  $S_{F,Th}$ .  $S_N$  is the power spectral density of measurement noise. Arrows indicate the half maximum.

Dissipation can be characterized by a quality factor, which is defined as the ratio between the total stored energy of a resonator and the energy lost per cycle:  $Q = 2\pi E/\Delta E$ . In terms of the displacement,  $Q$  is a dimensionless constant describing exponential decay:  $U(z, t) = \sum_{n=1}^{\infty} r_n u_n(z) e^{i\omega_n t} e^{-\omega_n t/(2Q_n)} = \sum_{n=1}^{\infty} U_n(z) e^{i(1+i/(2Q_n))\omega_n t}$ . Hence, we see that dissipation can be incorporated by defining a new eigenfrequency equal to  $(1 + i/2Q_n)\omega_n$ .

Mechanical force sensors sensitively transduce forces and force gradients into a change of displacement or resonance frequency. To explain this in more detail, we now introduce transverse driving forces of the form  $F(z, t) = F_0(z) e^{i\omega_d t}$ . For times long compared to transient time scales ( $t \gg Q_n/\omega_n$ ), the displacement of the beam follows the driving force and has the form  $U(z, t) = \sum_{n=1}^{\infty} r_n u_n(z) e^{i\omega_d t}$ . In the following, we only consider the motion of the free end ( $z = L$ ) of the cantilever. By adding  $F(L, t)$  to the right-hand-side of equation (1), we can evaluate the complex displacement response of the free end of the cantilever as a function of driving frequency  $\omega_d$  as:

$$r_n(\omega_d) = F(\omega_d) \chi_n(\omega_d) \equiv \frac{F(\omega_d)}{m_{n,eff} \omega_n^2 - \omega_d^2 + i\omega_d^2/Q_n}. \quad (4)$$

Here  $F(\omega_d)$  is the Fourier transform of  $F(L, t)$  and  $\chi_n(\omega_d)$  the mechanical susceptibility of the NW cantilever. Note that the displacement response given by the mode shapes requires the use of a mode-dependent effective mass  $m_{n,eff}$  rather than the cantilever mass in describing the dynamical behavior of the cantilever. This can be understood by considering that elements of the beam located closer to its clamped end react to a transverse force as if the local mass were higher than for elements closer to the free end. In fact, the effective mass is

**Table 2.** Wave numbers  $\beta_n$  and normalized eigenfrequencies  $\omega_n$  of a singly-clamped beam.

$n$	$\beta_n$	$\omega_n/\omega_0$
0	1.875	1.000
1	4.694	6.267
2	7.855	17.547
3	10.996	34.386
$n \geq 3$	$(n + 1/2)\pi$	$[(n + 1/2)\pi/\beta_0]^2$

proportional to the square of the mode volume  $m_{n,eff} = \frac{1}{|u_n(z_0)|^2} \int \rho(z) |u_n(z)|^2 dV$  and hence depends on the chosen normalization of  $u_n(z)$  [33]. Furthermore,  $m_{n,eff}$  depends on the position along the beam  $z_0$  for which motion is evaluated. For the fundamental flexural mode using our normalization condition  $|u_n(L)| = 1$ , it has a minimum of  $m_{0,eff} = M/4$  for  $z_0 = L$ , with  $M$  the cantilever mass. From here on we will use the notation  $m \equiv m_{0,eff}$ . Interestingly, equation (4) differs only slightly from the response of a simple harmonic oscillator, for which  $i\omega_n^2/Q_n$  is replaced by  $i\omega_d \omega_n/Q_n$ . The difference is negligible for large values of  $Q_n$  and disappears when driving on resonance.

In the following, we will therefore approximate the dynamics of a mode of a singly-clamped NW cantilever with that of a driven damped harmonic oscillator, considering only the displacement of the free end of the NW and assuming near-resonant driving. For simplicity, we only consider the fundamental flexural mode (typically the only one used in force sensing) and consequently we drop the subscript  $n$  (with the exception of  $\omega_0$ ). For small NW oscillation amplitudes, we

can approximate the force  $F$  acting on the NW around its equilibrium displacement  $r = 0$  as  $F \approx F(0) + rF_r$ , with  $F_r \equiv \partial F / \partial r|_0$ . Writing the displacement  $r(t)$  of the tip of the nanowire in an equation of motion of a damped driven harmonic oscillator, we obtain:

$$m\ddot{r} + \Gamma\dot{r} + (k - F_r)r = F(0) + F_{Th}, \quad (5)$$

where  $k$  is the mode spring constant and dots indicate differentiation with respect to time. We see that spatial derivatives  $F_r$  of forces acting on the NW modify the effective spring constant of the NW. Stationary forces acting on the NW provide a static offset of the cantilever displacement, whereas time-dependent forces can drive the motion of the NW and change its displacement amplitude, through the spectral transfer function of the resonance shown in equation (4). The aim of most force sensing experiments is the measurement of the forces  $F(0)$  and force derivatives  $F_r$ .

The remaining terms in equation (5),  $\Gamma\dot{r}$  and  $F_{Th}$ , correspond to dissipation and thermal force noise, respectively. Forces acting on the resonator typically do not only arise from controlled interactions, but also include components originating from the cantilever being in contact with a thermal bath. The noise in the resonator motion that results from this interaction is observable in the most sensitive force sensing measurements and is what typically sets the limit to their sensitivity. We include further terms in the equation of motion that account for energy dissipation and noise arising from the resonator being in contact with a largely uncontrolled and fluctuating environment of temperature  $T$ . This environment consists of a large number of degrees of freedom, such as those describing the motion of the molecules in the (typically highly diluted) fluid through which the nanowire moves and the phonon bath in the substrate to which the NW is attached through its clamping point. We use a statistical approach to include these effects in the equation of motion. The interactions with the environment can be decomposed into a rapidly fluctuating thermal force noise term  $F_{Th}$  and a slowly varying dissipation term proportional to the velocity of the resonator,  $\Gamma\dot{r}$  (see [34]), with  $\Gamma = m\omega_0/Q$ . While in thermal equilibrium, these two terms are related through the fluctuation-dissipation theorem [35], resulting in:

$$\Gamma = \frac{1}{2k_B T} \int_{-\infty}^{\infty} \langle F_{Th}(t)F_{Th}(t+s) \rangle ds, \quad (6)$$

where  $k_B$  is the Boltzmann constant and the brackets  $\langle \dots \rangle$  indicate that an ensemble average is taken, here used in the correlation function  $\langle F_{Th}(t)F_{Th}(t+s) \rangle$ , with  $t$  and  $t+s$  different points in time. To further describe the fluctuating force term  $F_{Th}(t)$ , we use the power spectral density (PSD). We define the force PSD  $S_F(\omega)$  as the Fourier transform of the force correlation function:

$$S_F(\omega) = 2 \int_{-\infty}^{\infty} \langle F(t)F(t+\tau) \rangle e^{i\omega\tau} d\tau, \quad \text{for } 0 < \omega < \infty. \quad (7)$$

Here  $S_F(\omega)$  is taken to be single-sided: since  $\langle F_{Th}(t)F_{Th}(t+s) \rangle$  is real, its Fourier transform is even. This allows us to only take into account positive values of  $\omega$  in

equation (7), provided we multiply the integral by 2. Furthermore, note that from the inverse Fourier transform of equation (7) we find that  $\langle F(t)^2 \rangle = \frac{1}{2\pi} \int_0^{\infty} S_F(\omega) d\omega$ . Correlations in a thermal bath (other than those taken into account for damping) usually exist only for extremely short times (typically  $< 10^{-13}$  s). Therefore, for thermal noise we can assume  $\langle F_{Th}(t)F_{Th}(t+s) \rangle = 2\Gamma k_B T \delta(s)$ , resulting in the white single-sided force PSD  $S_{F,Th} = 4k_B T \Gamma$ .

The single-sided displacement PSD  $S_r(\omega)$  can be similarly expressed by combining the amplitude response function of equation (4) with equation (7) as:

$$\begin{aligned} S_r(\omega) &= 2 \int_{-\infty}^{\infty} \langle r(t)r(t+\tau) \rangle e^{i\omega\tau} d\tau, \quad \text{for } 0 < \omega < \infty \\ &= S_F(\omega) |\chi|^2(\omega) = \frac{S_F(\omega)}{m^2} \frac{1}{(\omega_0^2 - \omega^2)^2 + \omega_0^4/Q^2}. \end{aligned} \quad (8)$$

We see that the mechanical resonator acts as a filter on the driving force, with  $\chi(\omega)$  the filter transfer function. An important example of this filtering effect is that spectrally white force noise results in displacement noise with a nearly Lorentzian spectrum with a maximum of  $S_{r,Th} = 4k_B T Q / m\omega_0^3$ . As discussed in section 3.1, this thermally induced displacement noise is what ultimately limits the sensitivity of force detection. Finally, we note that thermally induced phase noise (see [32, 36] for a thorough treatment) similarly limits the frequency stability of a mechanical resonator [37].

## 2.2. Linear motion of two orthogonal modes

For any cross-section that is symmetric around its center point, the moments of inertia  $I_x$  and  $I_y$  are equal, resulting in degenerate eigenmodes. The flexural oscillation direction in the plane is arbitrary in this case. Then the formalism of a single mode direction as discussed in the previous subsection suffices to describe the motion. However, small asymmetries in the cross-section or in the clamping conditions [21] lift this degeneracy and split each mode into a doublet of modes oscillating along orthogonal directions  $\hat{\mathbf{r}}_1$  and  $\hat{\mathbf{r}}_2$  (see figure 2). For the fundamental flexural mode of NW cantilevers, this results in a doublet with resonance frequencies that are typically split by a small fraction of these frequencies, but many times their linewidths. Several groups working with NW force sensors have observed orthogonal modes with frequency splittings of the order of  $10^3 - 10^4$  Hz. Moreover, similar orthogonal flexural modes can arise in doubly-clamped beams and have been observed, for example, in carbon nanotubes and SiN etched beams [38–40]. The use of such mode doublets as a way to realize bidimensional force sensing forms a major motivation for using NW cantilevers as force transducers and we will treat it in detail in this review. The mechanical dynamics of these mode doublets are very similar to that of two coupled modes and we can therefore apply the formalism of the previous subsection generalized to two modes.

Taking into account both orthogonal modes, the equation of motion can now be written in vectorial form as:

$$m\ddot{\mathbf{r}} + \mathbf{\Gamma} \cdot \dot{\mathbf{r}} + \mathbf{K} \cdot \mathbf{r} = \mathbf{F}(0) + \mathbf{F}_{Th}. \quad (9)$$

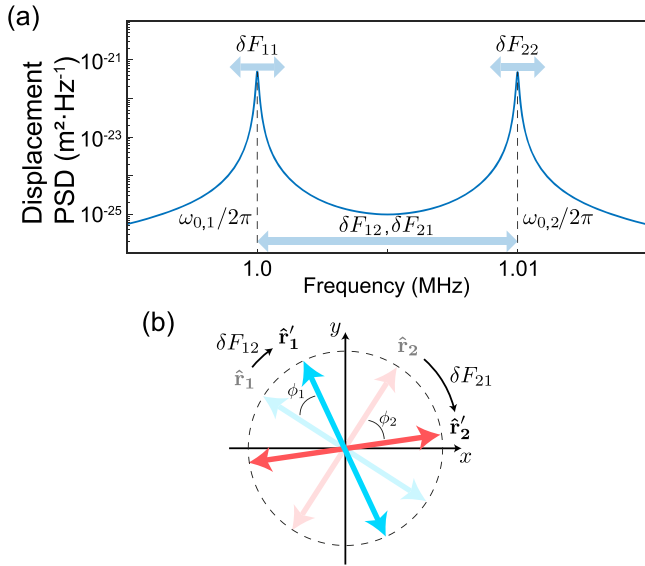


**Figure 2.** (a) Plot of thermal displacement PSD of a nearly-degenerate mode doublet. Arrows indicate the effect of the force derivatives  $F_{ij}$  on the resonant frequencies. (b) Schematic picture of rotation of mode directions under the influence of off-diagonal force derivatives  $F_{12}$  and  $F_{21}$ . Modes 1, 2 oscillate in the directions of the unit vectors  $\hat{\mathbf{r}}_{1,2}$ . The force derivatives  $\delta F_{12}$  and  $\delta F_{21}$  rotate the mode oscillation directions to point along the new unit vectors  $\hat{\mathbf{r}}'_{1,2}$ .

Here the displacement and forces are vectors defined in the basis of the two mode directions  $\hat{\mathbf{r}}_1$  and  $\hat{\mathbf{r}}_2$ , i.e.  $\mathbf{r} \equiv \begin{pmatrix} r_1 \\ r_2 \end{pmatrix}$ ,

$\mathbf{F}(0) \equiv \begin{pmatrix} F_1(0) \\ F_2(0) \end{pmatrix}$ , and  $\mathbf{F}_{Th} \equiv \begin{pmatrix} F_{Th,1} \\ F_{Th,2} \end{pmatrix}$ . The effective mass  $m$  is taken to be equal for the two modes (see for experimental verification of this the supplementary information of [1]), and  $r_i$  are the mode displacements.  $F_{Th,i}$  and  $F_i$  represent thermal force noise and other external forces acting on each of the two modes, respectively. We use the small-displacement approximation around  $r_i = 0$ ,  $F_i \approx F_i(0) + r_j \frac{\partial F_i}{\partial r_j}|_0$ . Furthermore, we define the dissipation and effective spring constant matrices  $\Gamma \equiv \begin{pmatrix} \Gamma_1 & 0 \\ 0 & \Gamma_2 \end{pmatrix}$  and  $\mathbf{K} \equiv \begin{pmatrix} k_1 - F_{11} & -F_{21} \\ -F_{12} & k_2 - F_{22} \end{pmatrix}$ . We write the four spatial force derivatives in shorthand notation as  $F_{ij} \equiv \frac{\partial F_i}{\partial r_j}|_0$ , with  $i, j \in \{1, 2\}$ .

We see that the force derivatives  $F_{ii}$  cause a change in the spring constant of each mode, similar to the single mode case. The off-diagonal elements of  $\mathbf{K}$  linearly couple the two modes, resulting in two new hybridized modes. The eigenvalues of the hybridized modes obtained by diagonalizing the  $\mathbf{K}$  matrix can be expressed as the modified spring constants (for  $\Gamma_i/2m \ll \sqrt{k_i/m}$ ):

$$k'_{1,2} = \frac{1}{2}[k_1 + k_2 - F_{11} - F_{22} \pm \sqrt{(k_1 - k_2 - F_{11} + F_{22})^2 + 4F_{12}F_{21}}]. \quad (10)$$

The modified eigenfrequencies then follow as  $\omega'_{0,i} = \sqrt{k'_{i}/m}$ . The directions of the corresponding new eigenmodes can be

written as:

$$\hat{\mathbf{r}}'_1 = \frac{1}{\sqrt{(k_2 - F_{22} - k'_1)^2 + F_{12}^2}} \begin{pmatrix} k_2 - F_{22} - k'_1 \\ F_{12} \end{pmatrix},$$

$$\hat{\mathbf{r}}'_2 = \frac{1}{\sqrt{(k_1 - F_{11} - k'_2)^2 + F_{21}^2}} \begin{pmatrix} F_{21} \\ k_1 - F_{11} - k'_2 \end{pmatrix} \quad (11)$$

We can further simplify (10) by making the assumption that the force derivatives are much smaller than the bare NW spring constants  $k_i$ , which is usually satisfied. This yields  $k'_i \approx k_i - F_{ii}$  and the following expression for the diagonal elements of the force derivative matrix:

$$F_{ii}|_{r_i=0} \approx -2k_i \Delta\omega_{0,i}/\omega_{0,i}. \quad (12)$$

Here  $\Delta\omega_{0,i}$  is the frequency shift of mode  $i$  induced by the force derivatives. Using the same approximation, the off-diagonal elements of the force derivative matrix (shear force derivatives) can be deduced from the angle  $\phi_i$  (see figure 2(b)) between the mode direction  $\hat{\mathbf{r}}'_i$  in the presence of the force derivatives and the bare mode direction  $\hat{\mathbf{r}}_i$  to be:

$$F_{ij}|_{r_i=0} \approx |k_i - k_j| \tan(\phi_i) \text{ for } i \neq j. \quad (13)$$

Note that in the situation where the NW cantilever is very soft and strong force derivatives are probed, these approximations are not valid and expressions for  $F_{ii}$  and  $F_{ij}$  remain slightly more complicated. In this case, the effects of the external force field dominate over the intrinsic NW mechanical properties, and the new eigenmodes tend to align with the eigenvectors of the force derivative matrix [16].

Equations (12) and (13) show that all in-plane force derivatives can be determined from measurements of the frequencies and oscillation angles of the two modes. The effect of  $F_{ij}$  on the two resonance frequencies is illustrated in figure 2(a). Finally, we note that the hybridized modes remain orthogonal as long as only conservative forces are included, in which case  $F_{12} = F_{21}$ . For forces with a finite curl, such as those arising from optical or frictional forces,  $F_{12} \neq F_{21}$  and orthogonality is not maintained. In this situation, the standard fluctuation-dissipation theorem is no longer a valid method of describing the interactions of the bimodal NW with a thermal environment and needs to be modified to include excess noise arising from the non-zero curl of  $\mathbf{F}$  [17]. An important further consequence of non-orthogonality is that it becomes impossible to distinguish a rotation of a mode from a change in mode temperature without a full vectorial read-out as described in section 3.2.

The forces  $\mathbf{F}$  and  $\mathbf{F}_{Th}$  are two-dimensional generalizations of the forces acting on a single mode. As for a single mode, stationary forces  $F_1$  and  $F_2$  yield a static offset in the NW displacement, now for each mode direction. Time-dependent forces drive the modes, leading to mode displacements given by a generalization of equation (4):

$$r'_i(\omega) = \mathbf{F}(\omega) \cdot \hat{\mathbf{r}}'_i \chi'_i(\omega) \text{ with } i, j \in \{1, 2\}, \quad (14)$$

with  $\hat{\mathbf{r}}'_i$  the unit vector along the oscillation direction and  $\chi'_i(\omega)$  the susceptibility of mode  $i$ , respectively. As described before, the force derivatives acting on the NW lead to the modified spring constants  $k'_i$  and mode directions  $\hat{\mathbf{r}}'_i$ , resulting

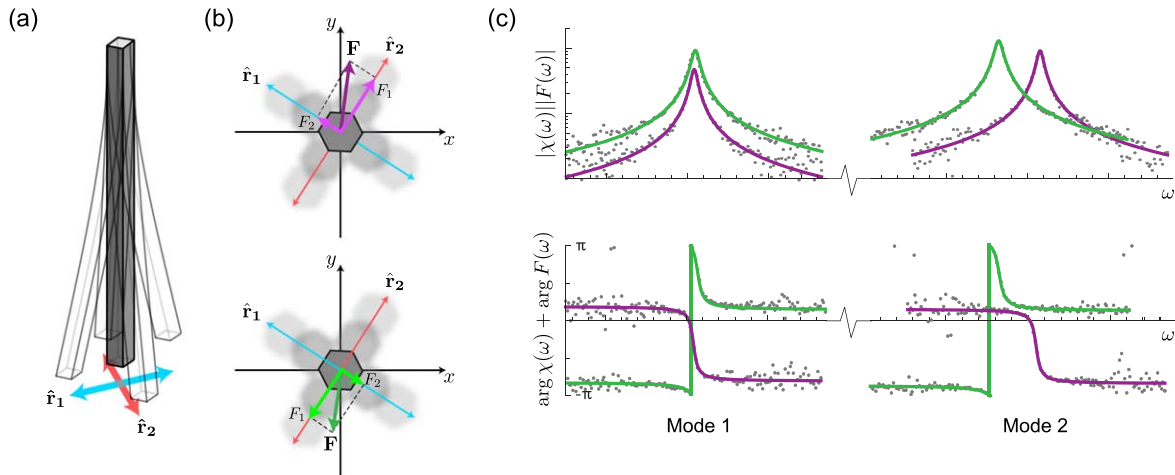


**Figure 3.** (a) Illustration of two orthogonal flexural modes in a NW cantilever. (b) Illustration of projection of vectorial forces onto mode directions, in the absence of spatial force derivatives. (c) Displacement amplitude and phase response of two modes as a function of driving frequency. The green and purple curves correspond to the response to the two forces indicated in (b) with the same colors. The displacement of each mode allows to extract the magnitude of the force component along that mode direction. The phase response of this mode with respect to the driving then allows to determine the sign of the force component along each mode direction. Reprinted by permission from Macmillan Publishers Ltd: [Nature Nanotechnology] [9], Copyright (2017).

in the new susceptibilities  $\chi'_i(\omega)$ . Figure 3(b) and (c) show how measurements of the displacement amplitudes and phases of both modes as a function of driving frequency can be used to reconstruct the full vectorial driving force.

### 2.3. Coherent two-mode dynamics

As mentioned in the above, the shear force derivatives  $F_{ij}$ , with  $i \neq j$ , couple the motion in the two modes. Interestingly, the resulting hybridized eigenmodes display coherent dynamics similar to that of quantum two-level systems. Coherent two-mode phenomena such as avoided mode crossings and Rabi oscillations have been observed in classical systems including modes of optical ring resonators [41] and recently also in nanomechanical resonators [39, 40, 42]. Furthermore, coupling of the orthogonal fundamental flexural modes of a NW cantilever was demonstrated through the measurement of avoided crossings of the mode frequencies [10], see figure 4(a). In the same experiment, Rabi oscillations were demonstrated through the use of time-dependent electric field derivatives, see figure 4(b). The NW was embedded in a scanning probe setup, which made it possible to tune both the coupling strength and the Rabi frequency by positioning the NW inside the electric field provided by the sample. Such coherent two-mode dynamics do not only illustrate the similarities of quantum and classical wave mechanics, but can also be used to enhance force sensing. In particular, coherent pulse sequences reminiscent from quantum control techniques [43], such as Hahn echoes and dynamical decoupling, give the potential to increase the frequency stability of mechanical sensors, ultimately leading to higher sensitivities. Furthermore, such pulsing techniques make it possible to implement a range of noise spectroscopy methods in classical force and mass sensing [43].

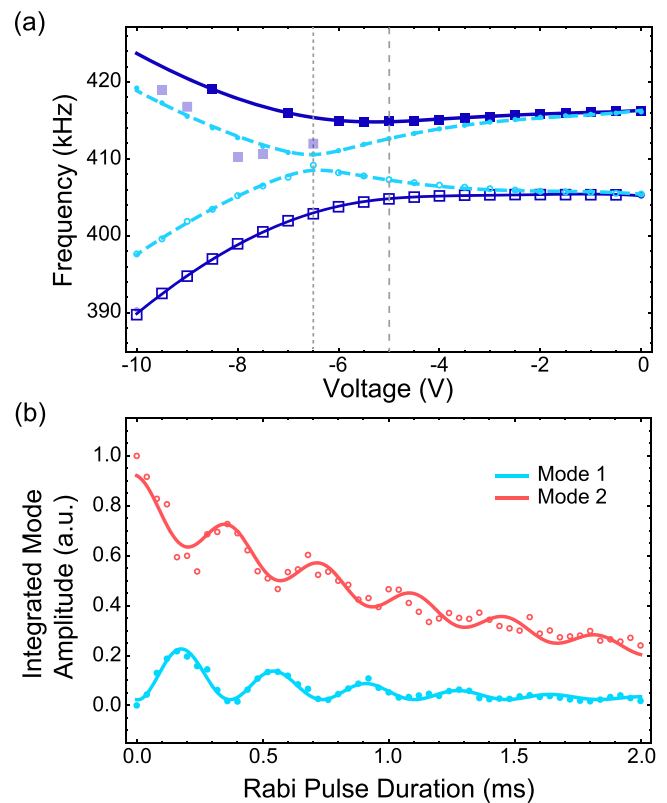


**Figure 4.** (a) Mode frequencies as a function of voltage applied over two nearby surface gates, for two different positions of the NW tip inside the electric field. (b) Integrated displacement amplitudes of both modes as a function of Rabi pulse duration. Points indicate measured data, solid lines are fits to the data. Note that the offset in the measured Rabi oscillations is due to thermal excitation of the mode. Different offsets result from the difference in angle of the two mode directions with the read-out vector. Reprinted with permission from [10], Copyright (2018) by the American Physical Society.

## 2.4. Nonlinear motion

In force sensing, nonlinear regimes of motion are typically avoided. However, in nanomechanical resonators such as NWs, nonlinear motion typically arises already for modest driving amplitudes and therefore needs to be considered. Moreover, nonlinearities can be put to good use, since they allow to implement amplification of forces through parametric driving [32] or through mechanical mixing [44]. Furthermore, parametric driving allows one to increase the ratio of transduced force signal to read-out noise [45]. In the last part of this section, we treat the situation in which the displacement of the NW cannot be considered to be small anymore and nonlinear terms need to be added to the equation of motion that depend on the oscillation amplitude.

It can be shown that for the fundamental flexural mode of a cantilever, the geometric nonlinearity, associated with the lengthening of the beam as it flexes, dominates over other nonlinearities, such as the inertial nonlinearity [46–48]. The first relevant higher-order terms are a damping term, as well as an effective spring constant term, that both have a quadratic dependence on the oscillation amplitude. For a single mode, this results in the following equation of motion [49]:

$$m\ddot{r} + \Gamma\dot{r} + \eta r^2\dot{r} + kr + \alpha r^3 = F(0) + F_{Th}(0) + F_r r. \quad (15)$$

The coefficient  $\alpha$  parametrizes the strength of the cubic (Duffing) nonlinearity, whereas  $\eta$  is the coefficient of nonlinear damping (note that here we contracted  $m$  into  $\alpha$  and  $\eta$ ). For weak damping and weak anharmonicity, other second- and third-order terms can be absorbed into the coefficients  $\alpha$  and  $\eta$  [50, 51]. The equation of motion (15) leads to an amplitude response as a function of driving frequency with a characteristic shark-fin shape, as shown in figure 5. This lineshape is a consequence of equation (15) having two stable solutions within a certain frequency range. This bistability leads to the switching phenomena seen for high driving amplitudes at the right flank of the response peak (figure 5(a)). Which of the two solutions is realized, is determined by the initial conditions, and mechanical hysteresis can be observed when adiabatically sweeping the driving frequency or driving amplitude up and down (figures 5(b) and (c)). When  $\alpha$  is positive (negative), the Duffing nonlinearity increases (decreases) the effective spring constant with increasing driving amplitude, thus stiffening (softening) the motion. The magnitude and sign of  $\alpha$  has been demonstrated to be tunable both through the shape of the NW [14], as well as through feedback using a nearby gate electrode [22]. The nonlinear damping term has the effect of decreasing the shift of the frequency of maximum response amplitude due to the Duffing nonlinearity, as well as decreasing the size of the hysteresis loop. Nonlinear damping has so far not been demonstrated for NW cantilevers. Finally, note that the dependence of mode frequencies on the displacement can lead to coupling between the two orthogonal modes. Considering only the Duffing nonlinearity, the nonlinear term for two modes becomes  $\alpha|\mathbf{r}|^2\mathbf{r}$ ; this term induces a coupling between two modes. The coupling can be observed as a quadratic shift

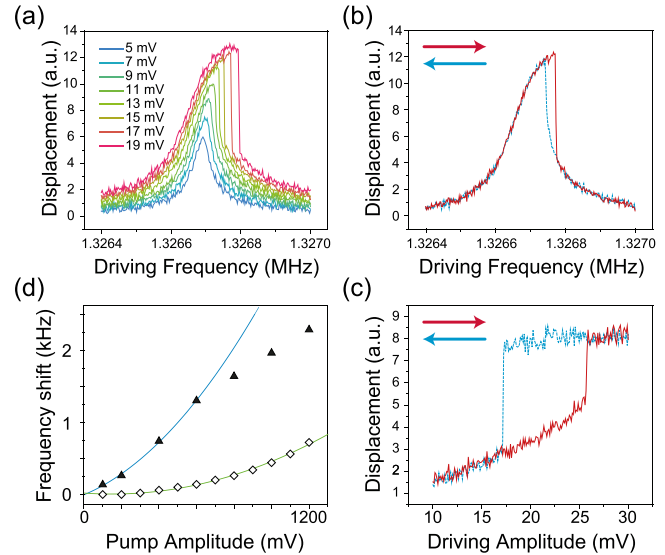


**Figure 5.** (a) Displacement as a function of driving frequency, for various amplitudes of piezoelectric driving. (b) Displacement as a function of driving frequency (at a driving amplitude of 17 mV), for two sweep directions (as indicated by arrows). (c) Displacement as a function of driving amplitude (at a driving frequency of 1.326 77 MHz), for two sweep directions. (d) Frequency shift of one mode as a function of amplitude of piezoelectric driving of orthogonal mode. Reprinted from [44], with the permission of AIP Publishing.

of a mode frequency as a function of the oscillation amplitude of the other mode (see figure 5(d)).

Notwithstanding its potential for force amplification, nonlinear motion has so far not been used in experiments on force sensing with NW cantilevers. In the following sections, we therefore only consider the operation of NW force transducers in a linear regime of motion.

## 3. Force sensing with nanowire cantilevers

### 3.1. Force sensitivity

The key component in any force microscope is the force sensor. This device consists of a mechanical transducer, used to convert force into displacement, and an optical or electrical displacement detector. Although early AFM transducers were simply pieces of gold or aluminum foil [52], specially designed and mass-produced Si cantilevers soon became the industry standard and led to improved resolution and force sensitivity [53]. These micro-processed devices are now cheap, readily available, and designed—depending on the target application—to have a variety of features including coatings, electrical contacts, or magnetic tips.

Conventional top-down cantilevers are well-suited for the measurement of the large forces and force gradients present on the atomic-scale. Nevertheless, for some applications sensitivity to small forces is crucial. These range from mass detection, to cantilever magnetometry, to scanning measurements of friction forces, Kelvin probe microscopy, electric force microscopy, magnetic force microscopy (MFM), and

force-detected magnetic resonance. This push towards higher sensitivity has generated an interest in using ever smaller mechanical force transducers, especially those made by bottom-up techniques.

The trend towards decreasing the size of mechanical transducers is based on fundamental principles. Once the detection of a transducer's displacement is optimized, the minimum detectable force  $F_{\min}$  is ultimately limited by the thermal force fluctuations acting on the transducer, whose PSD, as discussed in section 2.1, is given by  $S_{F,th}$ . As a result,

$$F_{\min} = \sqrt{S_{F,th}} = \sqrt{4k_B T \Gamma}, \quad (16)$$

Optimizing sensitivity therefore involves reducing the operating temperature and the dissipation. Note that efforts aimed purely at increasing mechanical quality factor may not necessarily minimize  $F_{\min}$ . Work on so-called 'damping dilution', uses tension applied to strings or membranes to increase resonant frequency  $\omega_0$  while holding  $\Gamma$  constant, thereby increasing  $Q$  [48, 54–57]. Although these methods do not improve  $F_{\min}$ , they do reduce the thermal decoherence time, which is important for experiments seeking to probe macroscopic quantum superposition states [58].

The sensitivity to a number of measurements is closely related to  $F_{\min}$  [59]. For example, the minimum detectable force gradient is given by  $(\partial F/\partial x)_{\min} = F_{\min}/x_{\text{osc}}$ , where  $x_{\text{osc}}$  is the root-mean-square oscillation amplitude of the transducer. Cantilever beams are also excellent torque transducers and, for some applications, torque is the measurement quantity of interest, e.g. in torque magnetometry. A cantilever's thermally limited torque sensitivity is given by  $\tau_{\min} = l_e F_{\min}$ , where  $l_e$  is the effective length of the cantilever, which takes into account the shape of the flexural mode [60]. Finally, for experiments that measure energy dissipation,  $\Gamma_{\min} = F_{\min}/(\omega_0 x_{\text{osc}})$ .

In practice, this means that at a given temperature, a well-designed cantilever transducer must simultaneously have low  $m\omega_0$  and large  $Q$ . In the limit of long and thin cantilever beams, the Euler–Bernoulli equations imply that  $m\omega_0 \propto d^3/l$ , where  $d$  is its diameter and  $l$  its length. For sensitive transducers, experiments show that  $Q$  is limited by surface-related losses, which lead to a linear decrease of  $Q$  with increasing surface-to-volume ratio, i.e.  $Q \propto d$  [61]. As a result, we see that  $\Gamma \propto d^2/l$ , implying that long and thin cantilevers should be the most sensitive. In fact, a review of real transducers confirms this trend.

High mechanical resonance frequencies are also attractive for sensitive force transducers, since they allow for the measurement of fast dynamics and they decouple the sensor from common sources of noise. A prominent example is the additional noise experienced by a cantilever as its tip approaches a surface [62, 63]. This so-called non-contact friction is largely due to electronic fluctuators on the surface and typically has a  $1/f$ -like frequency dependence. As a cantilever approaches a surface,  $\Gamma$  usually increases and its force resolution suffers. Such processes can be mitigated through the use of high-frequency cantilevers. When the resonant frequency of the mechanical oscillator is much higher than the characteristic frequency of the external noise, the resonator can be effectively decoupled from that noise.

A cantilever's angular resonance frequency is given by  $\omega_0 \propto d/l^2$ . Therefore, if we scale each of its dimensions uniformly by a factor  $\beta$ , we find that  $\omega_0 \propto 1/\beta$ , while  $\Gamma \propto \beta$ . Therefore, in order to simultaneously maximize  $\omega_0$  and minimize  $\Gamma$ , the entire structure should be scaled down.  $F_{\min} \propto \beta^{1/2}$ , and because of the additional contribution of the cantilever's effective length  $l_e \propto \beta$ ,  $\tau_{\min} \propto \beta^{3/2}$ . Reducing all dimensions while preserving the aspect ratio of a long and thin cantilever beam should thus optimize its ultimate force and torque sensitivity. This necessity for further miniaturization has positioned bottom-up techniques as the fabrication methods of the future.

In recent years, remarkable progress has been made in this direction with force sensors made from doubly-clamped CNTs [64], suspended graphene sheets [65], and NW cantilevers [1, 9, 16]. In two separate papers, Moser *et al* demonstrated the use of a CNT as a sensitive force sensor with a thermally limited force sensitivity of  $12 \text{ zN}/\sqrt{\text{Hz}}$  at 1.2 K in 2013 [38] and then of  $1 \text{ zN}/\sqrt{\text{Hz}}$  at 44 mK in 2014 [66]. Given their geometry, graphene resonators are extremely difficult to apply in scanning probe applications. Singly-clamped NWs and CNTs on the other hand, when arranged in the pendulum geometry—that is, with their long axes perpendicular to the sample surface—are well-suited as scanning probes. Their orientation prevents the tip from snapping into contact [67]. When brought close to a surface, NWs experience extremely low non-contact friction [6], making near-surface ( $<100 \text{ nm}$ ) force sensitivities around  $1 \text{ aN}/\sqrt{\text{Hz}}$ . As a result, NWs have already been used as scanning probes in a variety of proof-of-principle experiments discussed in section 4.

### 3.2. Displacement detection

As discussed above, the force transducer sets the fundamental sensitivity limits of any force sensor. However, for a force to be measured, the transducer's displacement must be detected. Therefore, in order to achieve the sensor's ultimate sensitivity, a displacement detection scheme sensitive enough to detect the transducers thermal motion is required. The displacement of conventional AFM cantilevers is measured through the deflection of a laser beam reflected off of the cantilever and onto a split photodetector. Although this scheme works well for cantilevers with flat surfaces large enough to specularly reflect a laser beam, it is not well-suited for NWs. Given their shape and sub-wavelength diameter, diffraction effects emerge and an alternative means of displacement detection must be employed.

To circumvent this challenge, researchers have developed a number of optical [25, 27, 68–71] and non-optical techniques, including electron beam [72], piezoresistive [73], magnetomotive [28], and capacitive [64, 74] displacement detection. None of these, however, are compatible with sensitive scanning probe microscopy (SPM) applications, in which the NW cantilever's thermal motion must be non-invasively detected while its tip is positioned close to the surface of a sample. Most recently, a pair of optical techniques based on optical interferometry or scattering have been

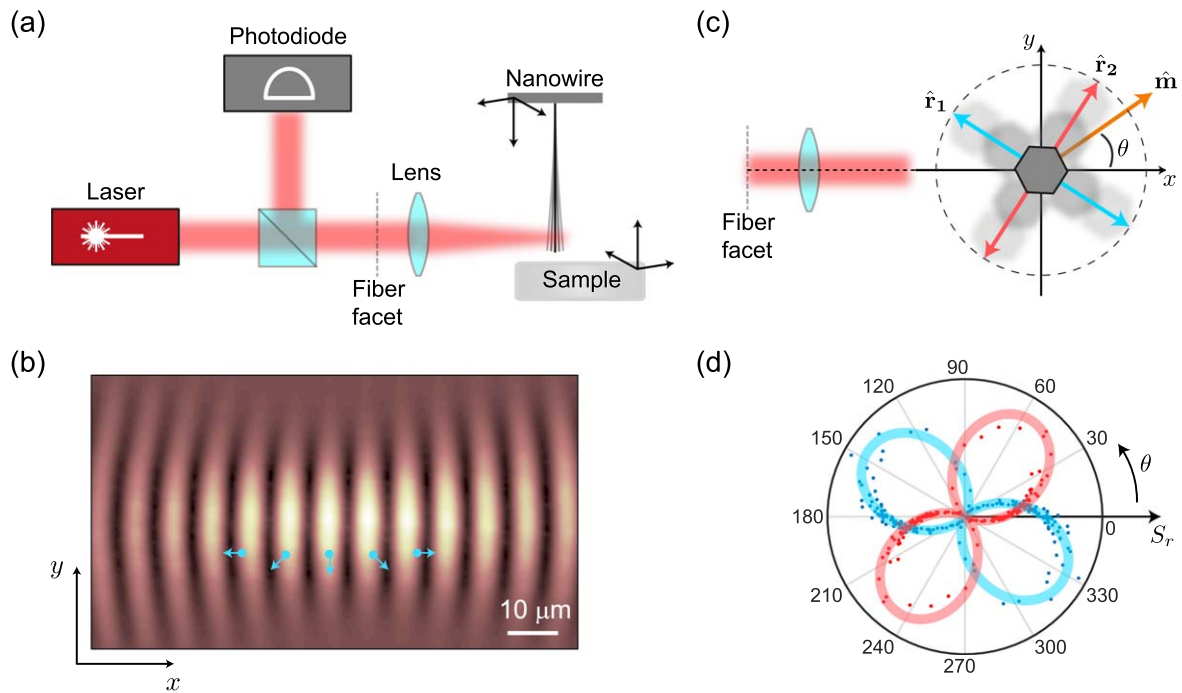


**Figure 6.** (a) Diagram of NW displacement detection setup. (b) Reflected intensity measured as a function of  $xy$  position of NW tip showing the interference fringes resulting from the low-finesse interferometer in the detection path. Arrows indicate the direction of the gradient of the intensity at different positions, determining the direction of the measurement vector. (c) Diagram illustrating mode directions and measurement vector. (d) NW displacement PSD as a function of measurement angle.

shown to be compatible with SPM applications, while at the same time providing access to both the amplitude and direction of the NW displacement [1, 9, 11, 16, 21]. A technique in which the electron beam in a scanning electron microscope (SEM) is focused on a cantilever and the inelastically scattered electrons are detected also resolved thermal displacement fluctuations of a singly-clamped CNT [31]. This scheme was subsequently integrated into a SPM with the CNT as the force transducer [29]. Due to its flexibility and relatively simple hardware required for its implementation, we will focus here on the optical techniques.

Using Mie scattering analysis, it can be shown that a NW positioned near the focus of an incident laser beam scatters sufficient light such that a measurement of optical transmission is sufficient to sensitively detect its displacement [75]. The technique uses the strong scattering intensity gradient as a function of the NW position in the plane perpendicular to its axis ( $xy$ -plane), to convert NW displacement into a change in optical transmission intensity  $I_T$ . The gradient of this intensity as a function of the NW position yields both the detection efficiency  $\epsilon = |\nabla I_T(x, y)|$  in  $\text{W m}^{-1}$  and the direction along which displacement is detected  $\hat{\mathbf{m}} = \nabla I_T(x, y) / |\nabla I_T(x, y)|$  [1]. The measured displacement is therefore a projection of the displacement of the two flexural modes  $m(t) = \hat{\mathbf{m}} \cdot (\mathbf{r}_1(t) + \mathbf{r}_2(t))$  along a direction that depends on the position of the NW in the beam waist. Using a split-photodiode detector, different response profiles can be obtained from the sum and difference of the two sensors. As a result, displacement signals along two perpendicular directions can be measured at the same time [16]. In this way, even with modest optical powers, the thermal displacement of the NW

modes can be measured in two-dimensions. The detection can be used to fully characterize the response of each set of doublet flexural modes to external forces and force gradients. Ultimately, this vectorial information allows for the reconstruction of the full, two-dimensional, force field acting on the NW. In addition, the relative orientation of the doublet, i.e. whether these modes oscillate orthogonal to each other or not, carries information about whether the force field in which the NW is immersed is conservative or not [17].

Another version of this detection scheme uses the interference between light scattered back from the NW and light reflected from the cleaved end of an optical fiber to measure NW displacement [11, 76]. In this case, a fiber-based confocal reflection microscope is used to collect the light scattered from the NW, as shown in figure 6(a). The fiber's end and the NW form a low-finesse Fabry–Perot cavity interferometer [9, 21], whose interferometric response depends on the position of the NW in the beam waist, as seen in figure 6(b). A fast photo-receiver monitors variations in the reflected intensity  $I_R$ , allowing for the sensitive detection of NW motion. As before, the efficiency  $\epsilon = |\nabla I_R(x, y)|$  and the direction of the detected displacement  $\hat{\mathbf{m}} = \nabla I_R(x, y) / |\nabla I_R(x, y)|$  depend on the variations of  $I_R$  as a function of the NW position in the optical waist [11]. In this case, along the cavity's axis,  $\nabla I_R$  depends on an interference effect and therefore can have a very high  $\epsilon$ , which can be improved by increasing the cavity finesse. Detection efficiency perpendicular to the cavity axis, on the other hand, depends on the narrowness of the optical waist. Using this method, the axis along which displacement is measured can be changed either by moving the NW within the optical waist or by tuning the laser excitation wavelength, which alters the interference pattern shown in figure 6(b).

As with the scattering based technique, this two-dimensional displacement detection technique allows for both angular and spectral tomography of a NW's flexural modes. As an example, the displacement power spectral density of a NW's thermally-excited fundamental mode doublet and its displacement power density as a function of the angle in the  $xy$ -plane are shown in figure 6(d).

Both the optical transmission and the interferometric techniques have been successfully integrated into a SPM using a single NW as the force transducer. Although technical restrictions exist, such that there is sufficient optical access to the NW (e.g. on the length of NW and the distance of the scanning region from the sample edge), setups can be designed to work with most samples of interest.

#### 4. Force microscopy with nanowire cantilevers

Recently, several proof-of-concept experiments have been performed that demonstrate the potential of force microscopy with NW cantilevers. First experiments focused on developing the optical detection of NW displacement [21, 25, 26] with high enough precision to observe the NW's thermo-mechanical noise, as well as on characterizing the mechanical properties of NW cantilevers [12, 22, 44]. The promise of ultra-low dissipation motivated researchers to implement NW cantilevers into scanning probe setups, for the sensitive detection of various types of forces. In a series of experiments [6, 7, 22], Nichol *et al* first used Si NWs as transducers in magnetic resonance force microscopy, exploiting their high mechanical frequencies and low dissipation to improve the sensitivity and resolution in measurements of small numbers of nuclear spins.

As mentioned before, when used in the pendulum geometry, NW cantilevers enable scanning probe microscopy of lateral forces. Such a mode of operation may be applied to, for example, the detection of frictional forces [4] or short-range non-central forces [77]. Although one-dimensional dynamic lateral force microscopy can be realized using the torsional mode of conventional AFM cantilevers [78–82], the ability to simultaneously image all vectorial components of nanoscale force fields is of great interest. Not only does it provide more information on tip-sample interactions, but it also enables the investigation of inherently 2D effects, such as the anisotropy or non-conservative character of specific interaction forces. Such vectorial force sensing has now been demonstrated for a variety of types of interaction.

The first implementation of a vectorial NW force sensor was realized by Gloppe *et al* [1] in an experiment where the optical force field of a laser beam focused onto a NW was mapped out. Optomechanical interactions lie at the basis of a very fruitful line of research in which quantum states of motion are studied using optical fields, for instance in optical resonators. To fully describe such optomechanical interactions, one needs to account for their non-conservative nature, and their spatial mapping necessitates the use of a fully vectorial force sensor, as described by Gloppe *et al*. Interestingly, this non-conservative character of the

optomechanical interaction can induce strong coupling between orthogonal mechanical modes, which can lead to non-trivial forms of back-action on the NW motion.

In a next step, vectorial NW force sensors were implemented in scanning probe setups, in which the NW cantilever could be scanned over a sample surface [9, 16]. These setups allowed for the measurement of two-dimensional maps of the sample surface, in which forces arising from Coulombic interactions, chemical bonding, and van der Waals interactions provide a topographic contrast. The NW cantilevers complement conventional AFM in providing a full determination of the four lateral force derivatives. Together, these experiments show the potential of NW cantilevers as ultra-sensitive bidimensional force transducers and provide experimental quantification of sensitivities and resolution. Force sensitivities were measured to be in the  $\text{aN Hz}^{-1/2}$  range. This is on par with or slightly better than sensitivities reached with conventional AFM. However, there is great potential for improvement of the force sensitivity, through optimization of NW geometry and surface properties. Spatial resolution was limited, as expected, by the NW tip diameter, which for these first experiments ranged between 100 and 350 nm. Also here, there is a clear route for improvement, since several types of NWs and nanotubes with tip diameters that are 10–100 times smaller have been grown.

A further exciting new development is the use of magnetic NW cantilevers or NWs with magnetic tips for sensitive and vectorial detection of magnetic forces. There are many current research topics that could be studied using MFM with NW cantilevers, including magnetic skyrmions, mesoscopic transport and quantum computation devices, and current flow in topologically non-trivial samples. First proof-of-principle results of NW MFM were obtained using a NW with a magnetic segment grown at its tip [11].

##### 4.1. Optical force sensing

Optical setups used to detect the displacement of a cantilever, based on either interferometry or scattering of light, can also be applied to study optomechanical interactions. The NW cantilever with its two orthogonal flexural modes gives the opportunity to investigate the vectorial nature of optomechanical coupling. Gloppe *et al* have performed such a study, by placing a NW cantilever inside the optical field of a laser beam tightly focused by a microscope objective with a high numerical aperture [1]. In this experiment, the optical intensity of the field was modulated with a frequency that was swept through both orthogonal mode resonant frequencies, providing driving forces through the optomechanical interaction. A second, much weaker laser beam was used to probe the thermal force noise of the NW, allowing the determination of the direction of the NW modes following the method outlined in section 2.2. The method of figure 3 was then used to acquire a map of the magnitude and direction of the in-plane optomechanical force. The force field of figure 7(a) shows a converging and diverging vector flow corresponding to the waist area of the focused laser beam. The optomechanical interaction is in general non-conservative and therefore the force field acting on the NW can

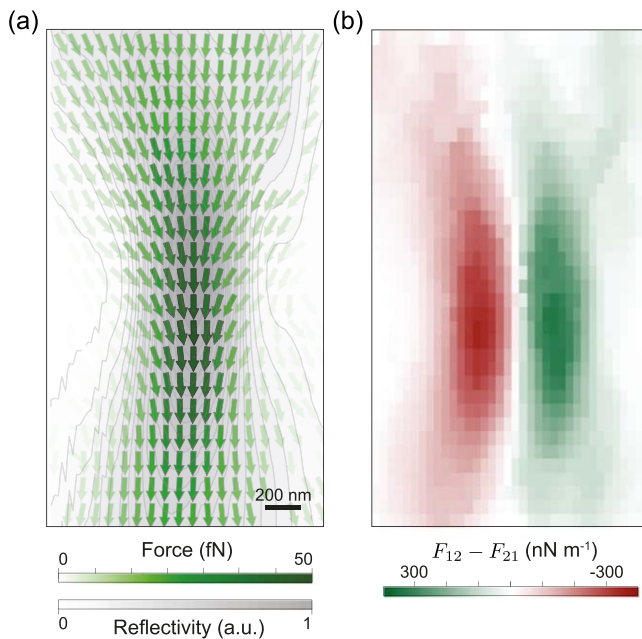


**Figure 7.** (a) Measured spatial map of optomechanical force field on NW tip placed inside focused laser beam. (b) Spatial map of the local curl derived from measurement displayed in (a). Reprinted by permission from Macmillan Publishers Ltd: [Nature Nanotechnology] [1], Copyright (2014).

possess a non-zero curl. The curl can be found by differentiating the vector force field and was determined to be maximum at the waist, on each side of the optical axis (see figure 7(b)). Furthermore, by measuring the delay between the laser intensity modulation and the NW response it was shown that the optomechanical force was in phase with the intensity modulation, as expected for a dissipative optomechanical coupling. The authors report a force sensitivity in the  $\text{aN Hz}^{-1/2}$  range at room temperature.

#### 4.2. Electrical force sensing

In scanning probe measurements of a sample surface, such as those made in conventional atomic force microscopy, the underlying sample-cantilever forces are typically of electrical origin. These forces include contributions from van der Waals forces and various other interactions of electrostatic origin. The measured forces closely follow the geometrical pattern of the sample surface, enabling the reconstruction of sample topography. In contrast to conventional AFM, NW cantilevers arranged in the pendulum geometry allow for the measurement of vectorial topographical maps of sample surfaces through the measurement of in-plane forces and force derivatives. In two experiments [9, 16], researchers recently demonstrated the use of NW cantilevers to measure such topographical maps.

Figure 8 shows various measurements involving a specific sample featuring 200 nm thick Au gate electrodes lithographically defined on a planar Si substrate. By scanning a NW cantilever over the sample surface, vectorial maps of the tip-sample forces and forces derivatives, as well as of the dissipation of both NW modes, were measured [9]. Figures 8(a)–(c) show maps of in-plane spatial force derivatives  $F_{11}$ ,  $F_{22}$ , and

$F_{12}$  (since electrical potentials are conservative, here  $F_{21} = F_{12}$ ), through measurements of the frequency shift and oscillation direction of the two orthogonal flexural modes of the NW. The measured in-plane force derivatives can be integrated to produce a map of in-plane tip-sample forces, up to an integration constant corresponding to a constant force in the plane. Figure 8(d) shows a map of the force field  $F_{int}$  extracted from such an integration and confirms that the measured forces are roughly perpendicular to the edges defined by the sample topography. Furthermore, figures 8(e)–(f) show maps of measured dissipations  $\Gamma_i$ , extracted from the mode linewidths. Dissipation was measured to be nearly isotropic in the plane and was affected mostly by the different materials and tip-sample spacing over electrodes and substrate. In principle, however, the demonstrated ability to produce vectorial maps of dissipation shows that NW cantilevers could find an application in the study of anisotropic non-contact friction, which is important for instance for the study of superlubricity [83].

In a next step, the authors generated an alternating electric field  $\mathbf{E}(\mathbf{r}, t)$  using the patterned electrodes to drive the motion of both NW modes. In this way, vectorial in-plane maps of the driving forces were obtained (see figures 8(g), (h)), with a thermally limited sensitivity of  $5 \text{ aN Hz}^{-1/2}$  at a temperature of 4 K. Two types of driving forces resulted from  $\mathbf{E}(\mathbf{r}, t)$ :  $\mathbf{F}_q = q\mathbf{E}$  and  $\mathbf{F}_p = -\nabla(\alpha|\mathbf{E}|^2)$ . Here  $q$  is the net charge on the NW tip and  $\alpha$  the polarizability of the NW. Since  $\mathbf{F}_q$  shows a linear dependence on the magnitude of the electric field, while that of  $\mathbf{F}_p$  is quadratic, these two forces are spectrally separated and could therefore be distinguished in measurement. Interestingly, such force measurements also allow the characterization of the NW itself. By comparing the magnitude of the measured forces with that of the applied electric field, the average values of the constants  $q$  and  $\alpha$  were determined.

In a similar setting, Mercier de Lépinay *et al* measured vectorial force fields and force field derivatives arising from the electrostatic interaction of a voltage-biased metallic sample of pyramidal shape with a NW cantilever [16]. The authors furthermore reconstructed a three-dimensional image of the force field derivatives by scanning the NW vertically away from the sample, up to a tip-sample distance of several microns.

#### 4.3. Magnetic force microscopy

In recent years, there has been a flurry of activity in developing nanometer-scale magnetic imaging technology. These efforts are driven by a number of outstanding questions in spintronics—such as how to control magnetic skyrmions—and in mesoscopic transport—such as how current flows in topological insulators and two-dimensional materials. Scanning probe microscopy, in particular, has made remarkable improvements in both the sensitivity and resolution of magnetic imaging. Some of the most successful tools are magnetic force microscopy (MFM), spin-polarized scanning tunneling microscopy, as well as scanning magnetometers based on nitrogen-vacancy centers in diamond, Hall-bars, and superconducting quantum interference devices (SQUIDs).

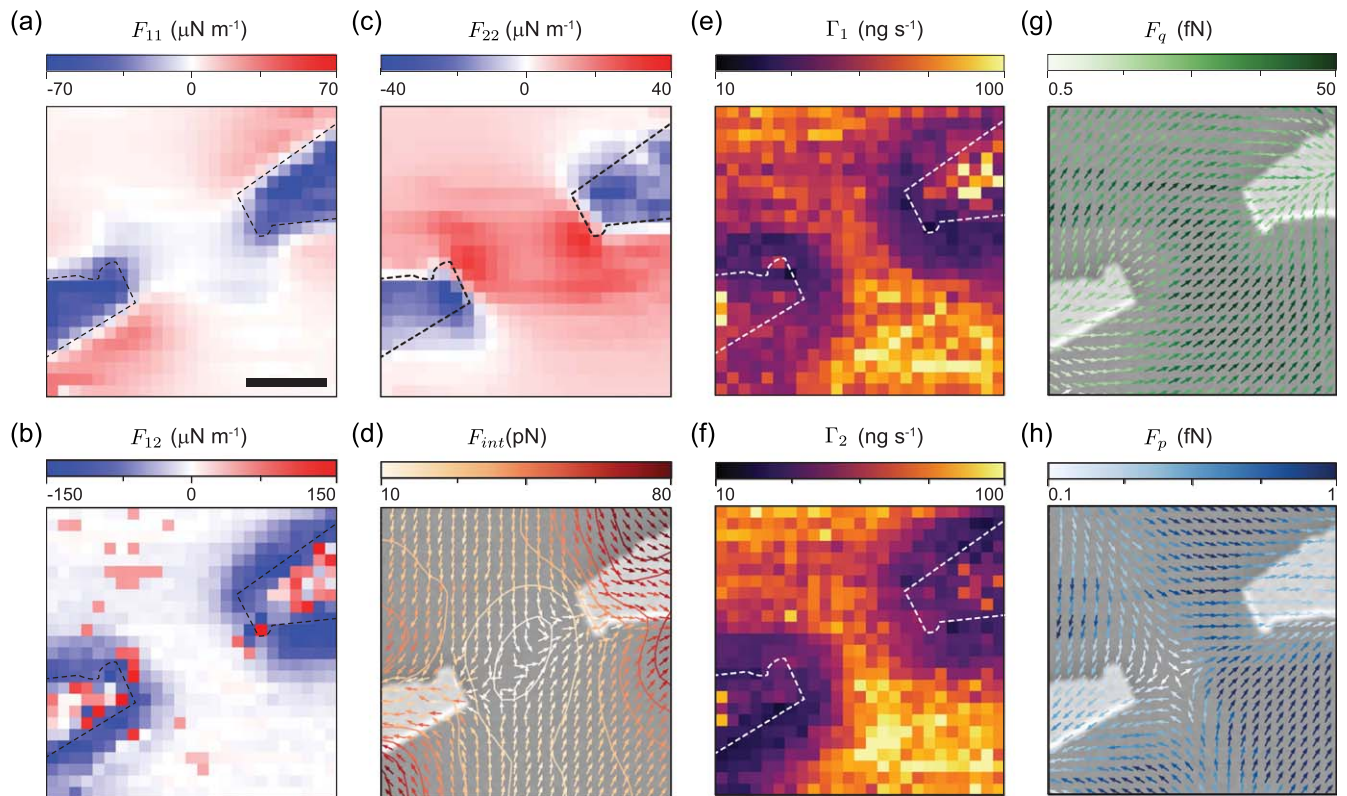


**Figure 8.** (a)–(c) Measurements of  $F_{11}$ ,  $F_{12}$ , and  $F_{22}$  tip-sample force derivatives as a function of NW tip position over patterned sample surface. The scale bar corresponds to  $1\ \mu\text{m}$  (d) Vector plot of in-plane force field derived by numerically integrating the derivatives of (a)–(c). The plot is overlaid on a scanning electron micrograph of the sample with patterned gate electrodes. (e), (f) Dissipation of each orthogonal mode as a function of NW tip position. (g) Vector plot of  $F_q$  induced by gate electric field on the charged NW. (h) Vector plot of  $F_p$  induced by gate electric field on the polarizable NW. Reprinted by permission from Macmillan Publishers Ltd: [Nature Nanotechnology] [9], Copyright (2017).

Despite this progress, it is now becoming clear that nano-mechanical sensors, in general, and NWs in particular, provide a huge untapped opportunity in magnetic sensing.

The first magnetic SPM, MFM, was introduced in the late 1980s as a natural extension of AFM. These days, it is performed in air, liquid, vacuum, and at a variety of temperatures. Under ideal conditions, state-of-the-art MFM can reach spatial resolutions down to  $10\ \text{nm}$  [84], though more typically around  $100\ \text{nm}$ . In 2009, its application to magnetic resonance, magnetic resonance force microscopy (MRFM), resulted in the first demonstration of three-dimensional nuclear magnetic resonance imaging (MRI) with nanometer-scale resolution [85].

NW scanning force sensors with proper functionalization of their tips, can be used to measure weak magnetic forces. Recent experiments have shown that a NW's high force sensitivity—when combined with a highly concentrated and strongly magnetized tip—gives it an exquisite sensitivity to magnetic field gradients [11]. Using a MnAs-tipped GaAs NW, Rossi *et al* demonstrated a sensitivity to  $11\ \text{mT}/(\text{m}\sqrt{\text{Hz}})$ . Having quantified the NW's response to magnetic field gradients, the authors calculate its sensitivity to other magnetic field sources, including a magnetic moment (dipole field), a superconducting vortex (monopole field), or an infinitely long and thin line of current [86]. In particular, they expect a moment sensitivity of  $54\ \mu_B/\sqrt{\text{Hz}}$ , a flux sensitivity of  $1.3\ \mu\Phi_0/\sqrt{\text{Hz}}$ , and line-

current sensitivity of  $9\ \text{nA}/\sqrt{\text{Hz}}$  at a tip-sample spacing of  $250\ \text{nm}$ . Such sensitivities compare favorably to those of other magnetic microscopies, including scanning Hall microscopy, magneto-optic microscopy, scanning SQUID microscopy, and scanning nitrogen-vacancy magnetometry. Furthermore, magnet-tipped NWs have a huge potential for improvement as probes of weak magnetic field patterns if tips sizes and tip-sample spacings can be further reduced.

In addition to improved sensitivity, NW MFM provides other potential advantages compared to conventional MFM. First, scanning in the pendulum geometry with the NW oscillating in the plane of the sample has the characteristics of lateral MFM. This technique, which is realized with the torsional mode of a conventional cantilever, distinguishes itself from the more commonly used tapping-mode MFM in its ability to produce magnetic images devoid of spurious topography-related contrast and in a demonstrated improvement in lateral spatial resolution of up to 15% [87]. Second, the nanometer-scale magnetic particle at the apex of the NW force sensor minimizes the size of the MFM tip, allowing for optimal spatial resolution and minimal perturbation of the investigated sample.

There have been a number of efforts at creating high-resolution MFM tips on conventional cantilevers, including attaching coated CNT tips [88], milling tips by FIB [89], or using electron beam induced deposition techniques [90, 91].

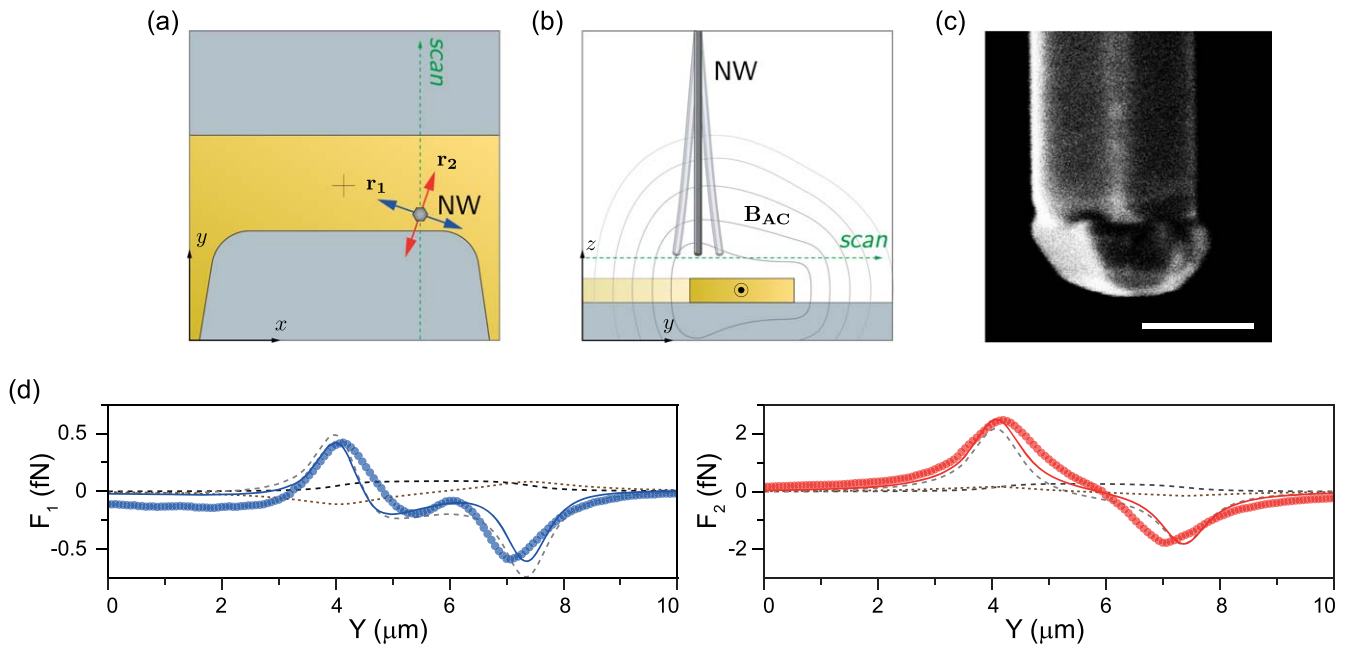


**Figure 9.** (a), (b) Schematic illustration of MFM experiment with NW cantilever and current-carrying Au wire. The NW scan direction used to produce measurements in (d) is indicated by the green line in top view (a) and side view (b).  $B_{AC}$  corresponds to the magnetic field produced by the alternating current in the wire and  $B$  to an externally applied magnetic field. (c) Scanning electron micrograph of the tip of a GaAs NW featuring a MnAs segment at the end. The scale bar corresponds to 100 nm. (d) Plots of the measured (dotted line) and calculated (solid line) forces driving the first (blue) and the second (red) mode over the line scan indicated in (a) and (b). For each plot three distinct drive contributions are shown as dashed lines: the monopole (black), dipole (gray) and torque (magenta) terms. Reprinted with permission from [11]. Copyright (2019) American Chemical Society.

Despite this work, non-invasive, high-resolution MFM tips are still needed. In particular, the tips with the smallest volumes realized thus far, tend to have rather undefined magnetization directions due to amorphous magnetic materials and nearly symmetric particle shape. Recent results show that small, single-crystal, magnetic particles with defined and predictable magnetization directions can be realized atop a single NW [11, 92]. In particular, Rossi *et al* carried out measurements of dynamic cantilever magnetometry [60, 93, 94] to extract the magnetic properties of each MnAs tip from the mechanical response of the NW to a uniform external magnetic field. These measurements, along with measurements of the NW's response to a well-known magnetic field profile generated by a lithographically patterned wire, confirmed that in remanence the magnetic tips are—in most cases—strongly magnetized and dipole-like. Figures 9(a) and (b) show the experimental setup in which the magnet-tipped NW is scanned across a current-carrying wire. An SEM of the MnAs magnetic tip is shown in figure 9(c). The magnetic force measured along the two mode directions is shown in figure 9(d), showing a response consistent with a remanent dipole-like magnetic tip. These results bode well for the resolution possible with NW MFM probes. In principle, as discussed by van Schendel *et al*, detailed analysis of MFM tips shows that the closer a tip approaches an ideal magnetic dipole, the better its sensitivity to high spatial frequencies, and therefore the higher its potential resolution [95].

The prospect of increased sensitivity and resolution, combined with few restrictions on operating temperature, make NW MFM ideally suited for investigating nanometer-scale spin textures, skyrmions, superconducting and magnetic

vortices, as well as ensembles of electronic or nuclear spins. Non-invasive magnetic tips may also open opportunities to study current flow in 2D materials and topological insulators. The ability of a NW sensor to map all in-plane spatial force derivatives [9, 16] should provide fine detail of stray field profiles above magnetic and current-carrying samples, in turn providing detailed information on the underlying phenomena. Directional measurements of dissipation may also prove useful for visualizing domain walls and other regions of inhomogeneous magnetization. As shown by Grütter *et al*, dissipation contrast, which maps the energy transfer between the tip and the sample, strongly depends on the sample's nanometer-scale magnetic structure [3].

#### 4.4. Magnetic resonance force microscopy

So far, the most developed application for magnetic force sensing with NWs has been MRFM for nanometer-scale magnetic resonance imaging (nano-MRI). The method relies on an ultra-sensitive mechanical force sensor to detect the magnetic resonance from tiny ensembles of nuclear spins.

Conventional MRI techniques employ pick-up coils to detect the small changes in magnetic field induced by flipping nuclear moments contained in a sample. These magnetic signals are so weak that conventional instruments cannot resolve objects smaller than several micrometers—about the size of a small cell [96]. MRFM improves on this sensitivity by mechanically detecting the magnetic forces produced by nuclear moments. A mechanical resonator is used to sense the forces arising between nuclear moments in a sample and a

nearby magnetic field gradient. In MRFM, RF pulses cause nuclear moments in a sample to periodically flip, generating an oscillating force on the mechanical resonator. These alternating forces, in turn, drive the resonator to oscillate. Force-detected MRI is more sensitive to nanometer-scale samples than conventional techniques because much smaller detectors can be made. For the inductive technique to be sensitive, the size of the pick-up coil must be similar to the size of the sample. For nanometer-scale samples, this is practically impossible. On the other hand, high-quality cantilevers can have dimensions far below a micrometer such that the sample mass is significant compared to the bare resonator mass. Such mechanical transducers enabled the current state-of-the-art force-detected nano-MRI, which was demonstrated by Degen *et al* in 2009 [85]. In this work, researchers captured 3D images of individual tobacco mosaic virus (TMV) particles with a resolution better than 10 nm along each dimension. The technique has the unique capability to image the interior of nanometer-scale objects non-invasively and with intrinsic chemical selectivity. Despite a number of further refinements and demonstrations [97, 98], improvements in MRFM sensitivity and resolution have stalled in recent years, leaving a number of technical obstacles to be overcome for the technique to become a useful tool for biologists and materials scientists.

Foremost among these obstacles is the reduction in the mechanical dissipation of the cantilever sensor. Lower mechanical dissipation would yield better force sensitivities and therefore sensitivity to smaller numbers of nuclear spins. Such an improvement would result in nano-MRI with improved resolution. In the last few years, the development and application of NW cantilevers to MRFM has been making promising steps in this direction. In 2012, Nichol *et al* used a Si NW force transducer in an MRFM experiment detecting  $^1\text{H}$  in a nanometer-scale polystyrene sample [6]. During the measurements they achieved a thermally limited force sensitivity of around  $1\text{aN}/\sqrt{\text{Hz}}$  at a spacing of 80 nm from the surface at 8 K, which is significantly lower than was measured at 300 mK in the TMV experiment [85]. This improvement is largely due to the ultra-low native dissipation of the NWs in comparison to top-down ultra-sensitive cantilever and to their drastically reduced surface dissipation. In fact, Nichol *et al* show that at a tip-surface spacing of 7 nm, a typical Si NW experiences nearly a factor of 80 less surface dissipation and factor of 250 less total dissipation than audio frequency cantilevers under similar conditions. The mechanisms behind this difference are not completely clear; the small cross-sectional area of a NW may decrease its coupling to the surface or, perhaps, the spectral density of surface fluctuations is lower at the MHz resonant frequencies of the NWs than at the kHz resonant frequencies of the cantilevers.

This ground-breaking work established NW oscillators as ultra-sensitive cantilevers for MRFM detection. The measurement protocol that was developed for the NW transducers uses a nanoscale current-carrying wire to generate both time-dependent RF magnetic fields and time-dependent magnetic field gradients. This protocol, known as MAGGIC, may

ultimately open new avenues for nanoscale magnetic resonance imaging with more favorable SNR properties [7].

Given that nanometer-scale MRFM requires intense static magnetic field gradients, both NMR spectroscopy and uniform spin manipulation using RF pulses have always been difficult to implement in such measurements. As a result, MRFM experiments often rely on inherently slow adiabatic passage pulses, which limited the mechanical transducer to resonance frequencies in the few kHz regime. In addition, conventional pulsed magnetic resonance techniques cannot be applied to nanometer-scale MRFM because statistical spin fluctuations often exceed the Boltzmann spin polarization [99]. In this regime, the projection of the sample magnetization along any axis fluctuates randomly in time.

In their article, Nichol *et al* presented a new paradigm in force-detected magnetic resonance that overcomes both challenges to enable pulsed nuclear magnetic resonance in nanometer-size statistically polarized samples. The first challenge was solved by using the nanometer-scale constriction to generate both large RF fields and large magnetic field gradients. In this way, the authors were able to turn their magnetic field gradients on and off at will. The method allowed the use of high-frequency mechanical resonances, such as those provided by a NW. Using a scheme similar to conventional MRI, switchable gradients in static and RF fields encoded the Fourier transform of the 2D spin density into their spin signal. As a result, they were able to reconstruct a 2D projection of the  $^1\text{H}$  density in a polystyrene sample with roughly 10-nm resolution. The protocol was able to function in the statistically polarized regime because the authors periodically applied RF pulses, which create correlations in the statistical polarization of a solid organic sample. The spin-noise correlations were then read-out using gradient pulses generated by ultra-high current densities in the nanoscale metal constriction. The authors also showed that Fourier transform imaging enhances sensitivity via the multiplex advantage for high-resolution imaging of statistically polarized samples. Most importantly, the protocol established a method by which all other pulsed magnetic resonance techniques can be used for nanoscale imaging and spectroscopy. Recent work by Rose *et al*, combines the high spin sensitivity of NW-based magnetic resonance detection with high-spectral-resolution NMR spectroscopy [8]. The authors make use of the resulting enhancement in nuclear spin coherence times to perform Fourier transform imaging of proton spins with a one-dimensional slice thickness below 2 nm.

Given the potential for even more sensitive NW transducers, these proof-of-concept experiments bode well for increasing nano-MRI sensitivity and resolution. Even without sensitivity improvements, the authors' technique could also be extended to enable full 3D encoding with constrictions capable of producing two orthogonal static gradients [100]. More generally, the approach serves as a model for applying sophisticated pulsed magnetic resonance schemes from conventional MRI to the nanometer-scale version.

## 5. Outlook

The application of NW cantilevers as sensitive force transducers is in the early stages. Nevertheless, the demand for more sensitive techniques has positioned nanometer-scale mechanical structures—and NWs in particular—as the transducers of the future. At present, the promise of these devices has been demonstrated in a small number of proof-of-concept experiments. As discussed in this review, these methods and applications demonstrate the capabilities of NW transducers and their unique advantages, especially in the detection of weak forces. Nevertheless, much work remains to be done before NWs become part of the standard tool-box of scanning probe microscopies.

Better spatial resolutions could be achieved by developing NWs with sharper tips, through, for example, specialized growth techniques or by focused ion beam milling. This could be pushed to obtain atomic resolution. Sharp NW tips ending in a single atom could be produced in the same way that such tips are produced for regular AFM, using oxidation sharpening [101, 102]. A second point that needs to be addressed to achieve atomic resolution is the amplitude of lateral displacement. Lateral oscillation amplitudes smaller than the spacing between adjacent sample surface atoms (typically a few Å) are obtained in regular lateral AFM by using very stiff cantilevers, such as a qPlus sensor [102], or a stiff torsional mode of a standard Si cantilever [77]. Similarly, stiff NWs could be used for this purpose. Additionally, feedback cooling [103] could be used to decrease thermal displacement amplitudes of less stiff NW cantilevers. Finally, experiments aiming for atomic resolution should be performed in ultra-high vacuum conditions. Combined with its vectorial force sensing capability, such a NW scanning probe could be used to reveal the anisotropy of atomic bonding forces.

Force sensitivity can undoubtedly be improved by developing longer and thinner NW transducers. So far, researchers have not made concerted efforts to optimize NW geometry, leaving much to be gained by such work. Further improvements in force sensitivity can be expected from the mitigation of surface-related dissipation processes. Even though such processes likely dominate the mechanical dissipation of NWs, detailed studies into characterization mitigation strategies have so far been sparse. Such studies could be combined with the development of growth methods optimized for producing high-quality NW cantilevers. In addition to surface-induced losses, dissipation related to the NW clamping point could potentially also be addressed through refined growth techniques and suitable patterning of the substrate to which the NW is attached. Moreover, high-finesse optical cavities could be used to enhance the signal-to-noise ratio of NW displacement detection through preferential scattering into cavity modes.

Higher force sensitivity would also translate into more sensitive measurements of dissipation and non-contact friction. AFM in the pendulum geometry—the same geometry used for NWs—is ideally suited to measurements of nanometer-scale dissipation. Such measurements have recently been used to detect superconducting [4] and bulk structural

phase transitions [104]. They can also shed light on concepts such as superlubricity, atomic-scale friction, and quantum friction [105]. Furthermore, energy dissipation plays a central role in the breakdown of topological protection, the loss of quantum information, and disorder-assisted hot electrons scattering in graphene [106]. The ability to map tip-sample force fields and energy losses makes NW transducers ideal for investigating how and where energy leaks.

The combination of high force sensitivity, high spatial resolution, and low invasiveness of magnetic NW probes has the potential to expand the applicability of MFM. Such sensors could image the stray field from thin ferromagnetic layers and other magnetic nanostructures hosting non-uniform states too fragile for conventional MFM. For such applications, efforts must first focus on producing smaller magnetic tips. Alternatively, the production of different types of magnet-tipped NWs could be attempted, through the evaporation of magnetic caps on sharp non-magnetic NWs or by direct focused ion beam induced deposition. The resulting improvement in spatial resolution, combined with the already demonstrated sensitivity to charge currents, could make magnet-tipped NWs ideal tools for mapping mesoscopic current flow. With the current sensitivity shown by Rossi *et al* it should be possible to detect with a bandwidth of 1 Hz the current flowing in a transport channel with a single quantum of conductance, when a reasonable bias voltage of order mV is applied over the channel. The quoted current sensitivity was limited by thermal displacement noise of the NW cantilever, which could also be improved by optimizing NW geometry. Such current sensitivities would enable imaging currents in quantum transport devices, such as gated quantum dots. Recent interest in imaging current densities in 2D materials and topological insulators has already driven the development of NV and SQUID based SPM, although much room for improvement remains, and NW cantilevers could find similar applications. In addition, by combining NW transducers with ferromagnetic resonance techniques, the spatial imaging of spin waves and the dynamics of individual skyrmions may also become possible.

Finally, viewed from a broader perspective, NW cantilevers hold potential for detection schemes beyond force sensing alone. In particular, NW and CNT cantilevers have been used as transducers for ultra-sensitive mass sensing experiments, leveraging their low mass, low spring constant, and vectorial character [23, 107–109] (Note that this list of references is by no means exhaustive). Another example is the hybridization of nanowires with self-assembled quantum dots. Such quantum dots host excitonic states which can be excited optically and which decay by emitting photons. The excitonic transition energies and amplitudes depend on local fields and can be used as sensitive and fast detectors of electric fields [110], strain gradients [111], and potentially also magnetic fields. The integration of such quantum dots within NW cantilevers allows for various types of SPM by monitoring the excitonic transition energy while scanning the NW over a sample.

## ORCID iDs

F R Braakman  <https://orcid.org/0000-0003-3442-0110>

M Poggio  <https://orcid.org/0000-0002-5327-051X>

## References

- [1] Gloppe A, Verlot P, Dupont-Ferrier E, Siria A, Poncharal P, Bachelier G, Vincent P and Arcizet O 2014 *Nat. Nanotechnol.* **9** 920–6
- [2] Thilloren N, Sebald K, Hardtdegen H, Meijers R, Calarco R, Montanari S, Kaluza N, Gutowski J and Lüth H 2006 *Nano Lett.* **6** 704–8
- [3] Grütter P, Liu Y, LeBlanc P and Dürig U 1997 *Appl. Phys. Lett.* **71** 279–81
- [4] Kisiel M, Gnecco E, Gysin U, Marot L, Rast S and Meyer E 2011 *Nat. Mater.* **10** 119–22
- [5] Cockins L, Miyahara Y, Bennett S D, Clerk A A and Grutter P 2012 *Nano Lett.* **12** 709–13
- [6] Nichol J M, Hemesath E R, Lauhon L J and Budakian R 2012 *Phys. Rev. B* **85** 054414
- [7] Nichol J M, Naibert T R, Hemesath E R, Lauhon L J and Budakian R 2013 *Phys. Rev. X* **3** 031016
- [8] Rose W, Haas H, Chen A Q, Jeon N, Lauhon L J, Cory D G and Budakian R 2018 *Phys. Rev. X* **8** 011030
- [9] Rossi N, Braakman F R, Cadeddu D, Vasyukov D, Tütüncüoğlu G, Fontcuberta i Morral A and Poggio M 2017 *Nat. Nanotechnol.* **12** 150–5
- [10] Braakman F R, Rossi N, Tütüncüoğlu G, Fontcuberta i Morral A and Poggio M 2018 *Phys. Rev. Appl.* **9** 054045
- [11] Rossi N, Gross B, Dirnberger F, Bougeard D and Poggio M 2019 *Nano Lett.* **19** 930–6
- [12] Cadeddu D, Braakman F R, Tütüncüoğlu G, Matteini F, Rüffer D, Fontcuberta i Morral A and Poggio M 2016 *Nano Lett.* **16** 926–31
- [13] Montinaro M, Wüst G, Munsch M, Fontana Y, Russo-Averchi E, Heiss M, Fontcuberta i Morral A, Warburton R J and Poggio M 2014 *Nano Lett.* **14** 4454–60
- [14] Foster A P, Maguire J K, Bradley J P, Lyons T P, Krysa A B, Fox A M, Skolnick M S and Wilson L R 2016 *Nano Lett.* **16** 7414–20
- [15] Pairis S, Donatini F, Hocevar M, Tumanov D, Vaish N, Claudon J, Poizat J P and Verlot P 2018 *Phys. Rev. Lett.* **122** 083603
- [16] de Lépinay L M, Pigeau B, Besga B, Vincent P, Poncharal P and Arcizet O 2017 *Nat. Nanotechnol.* **12** 156–62
- [17] de Lépinay L M, Pigeau B, Besga B and Arcizet O 2018 *Nat. Commun.* **9** 1401
- [18] Perisanu S, Vincent P, Ayari A, Choueib M, Purcell S T, Bechelany M and Cornu D 2007 *Appl. Phys. Lett.* **90** 043113
- [19] Perisanu S, Barois T, Ayari A, Poncharal P, Choueib M, Purcell S T and Vincent P 2010 *Phys. Rev. B* **81** 165440
- [20] Pigeau B, Rohr S, Mercier de Lépinay L, Gloppe A, Jacques V and Arcizet O 2015 *Nat. Commun.* **6** 8603
- [21] Nichol J M, Hemesath E R, Lauhon L J and Budakian R 2008 *Appl. Phys. Lett.* **93** 193110
- [22] Nichol J M, Hemesath E R, Lauhon L J and Budakian R 2009 *Appl. Phys. Lett.* **95** 123116
- [23] Gil-Santos E, Ramos D, Martínez J, Fernández-Regúlez M, García R, San Paulo A, Calleja M and Tamayo J 2010 *Nat. Nanotechnol.* **5** 641–5
- [24] Gil-Santos E, Ramos D, Pini V, Llorens J, Fernández-Regúlez M, Calleja M, Tamayo J and Paulo A S 2013 *New J. Phys.* **15** 035001
- [25] Ramos D, Gil-Santos E, Pini V, Llorens J M, Fernández-Regúlez M, San Paulo A, Calleja M and Tamayo J 2012 *Nano Lett.* **12** 932–7
- [26] Ramos D, Gil-Santos E, Malvar O, Llorens J M, Pini V, Paulo A S, Calleja M and Tamayo J 2013 *Sci. Rep.* **3** 3445
- [27] Belov M, Qitoriano N J, Sharma S, Hiebert W K, Kamins T I and Evoy S 2008 *J. Appl. Phys.* **103** 074304
- [28] Feng X L, He R, Yang P and Roukes M L 2007 *Nano Lett.* **7** 1953–9
- [29] Siria A and Niguès A 2017 *Sci. Rep.* **7** 11595
- [30] Tavernarakis A, Stavrinadis A, Nowak A, Tsioutsios I, Bachtold A and Verlot P 2018 *Nat. Commun.* **9** 662
- [31] Tsioutsios I, Tavernarakis A, Osmond J, Verlot P and Bachtold A 2017 *Nano Lett.* **17** 1748–55
- [32] Cleland A N 2003 *Foundations of Nanomechanics From Solid-State Theory to Device Applications* (Berlin: Springer)
- [33] Poot M and van der Zant H S J 2012 *Phys. Rep.* **511** 273–335
- [34] Reif F 1965 *Fundamentals of Statistical and Thermal Physics (McGraw-Hill Series in Fundamentals of Physics)* (New York: McGraw-Hill)
- [35] Kubo R 1966 *Rep. Prog. Phys.* **29** 255
- [36] Robins W P 1982 *Phase Noise in Signal Sources: (Theory and Applications) (IEE Telecommunications Series)* (London: Peregrinus)
- [37] Sansa M *et al* 2016 *Nat. Nano.* **11** 552–8
- [38] Moser J, Güttinger J, Eichler A, Esplandiu M J, Liu D E, Dykman M I and Bachtold A 2013 *Nat. Nanotechnol.* **8** 493–6
- [39] Faust T, Rieger J, Seitner M J, Krenn P, Kotthaus J P and Weig E M 2012 *Phys. Rev. Lett.* **109** 037205
- [40] Faust T, Rieger J, Seitner M J, Kotthaus J P and Weig E M 2013 *Nat. Phys.* **9** 485–8
- [41] Spreew R J C, van Druten N J, Beijersbergen M W, Eliel E R and Woerdman J P 1990 *Phys. Rev. Lett.* **65** 2642–5
- [42] Okamoto H, Gourgout A, Chang C Y, Onomitsu K, Mahboob I, Chang E Y and Yamaguchi H 2013 *Nat. Phys.* **9** 480–4
- [43] Degen C L, Reinhard F and Cappellaro P 2017 *Rev. Mod. Phys.* **89** 035002
- [44] Braakman F R, Cadeddu D, Tütüncüoğlu G, Matteini F, Rüffer D, i Morral A F and Poggio M 2014 *Appl. Phys. Lett.* **105** 173111
- [45] Eichler A, Heugel T L, Leuch A, Degen C L, Chitra R and Zilberberg O 2018 *Appl. Phys. Lett.* **112** 233105
- [46] da Silva M R M C and Glynn C C 1978 *J. Struct. Mech.* **6** 449–61
- [47] da Silva M R M C and Glynn C C 1978 *J. Struct. Mech.* **6** 437–48
- [48] Schmid S, Villanueva L G and Roukes M L 2016 *Fundamentals of Nanomechanical Resonators* (Switzerland: Springer International Publishing)
- [49] Cadeddu D 2018 *Nanomechanics and scanning probe microscopy with nanowires PhD Thesis* University of Basel
- [50] Lifshitz R and Cross M C 2008 *Rev. Nonlinear Dyn. Complexity* **1** 1–52
- [51] Eichler A, Moser J, Chaste J, Zdrojek M, Wilson-Rae I and Bachtold A 2011 *Nat. Nanotechnol.* **6** 339–42
- [52] Rugar D and Hansma P 2008 *Phys. Today* **43** 23
- [53] Akamine S, Barrett R C and Quate C F 1990 *Appl. Phys. Lett.* **57** 316–8
- [54] González G I and Saulson P R 1994 *J. Acoust. Soc. Am.* **96** 207–12
- [55] Cagnoli G, Hough J, DeBra D, Fejer M M, Gustafson E, Rowan S and Mitrofanov V 2000 *Phys. Lett. A* **272** 39–45
- [56] Tsaturyan Y, Barg A, Polzik E S and Schliesser A 2017 *Nat. Nanotechnol.* **12** 776–83

- [57] Ghadimi A H, Fedorov S A, Engelsen N J, Bereyhi M J, Schilling R, Wilson D J and Kippenberg T J 2018 *Science* **360** 764–8
- [58] Marshall W, Simon C, Penrose R and Bouwmeester D 2003 *Phys. Rev. Lett.* **91** 130401
- [59] Rugar D, Stipe B C, Mamin H J, Yannoni C S, Stowe T D, Yasumura K Y and Kenny T W 2001 *Appl. Phys. A* **72** S3–10
- [60] Stipe B C, Mamin H J, Stowe T D, Kenny T W and Rugar D 2001 *Phys. Rev. Lett.* **86** 2874–7 00111
- [61] Tao Y, Navaretti P, Hauert R, Grob U, Poggio M and Degen C L 2015 *Nanotechnology* **26** 465501
- [62] Stipe B C, Mamin H J, Stowe T D, Kenny T W and Rugar D 2001 *Phys. Rev. Lett.* **87** 096801
- [63] Kuehn S, Loring R F and Marohn J A 2006 *Phys. Rev. Lett.* **96** 156103
- [64] Sazonova V, Yaish Y, Üstünel H, Roundy D, Arias T A and McEuen P L 2004 *Nature* **431** 284–7
- [65] Bunch J S, van der Zande A M, Verbridge S S, Frank I W, Tanenbaum D M, Parpia J M, Craighead H G and McEuen P L 2007 *Science* **315** 490–3
- [66] Moser J, Eichler A, Güttinger J, Dykman M I and Bachtold A 2014 *Nat. Nanotechnol.* **12** 1007–11
- [67] Gysin U, Rast S, Kisiel M, Werle C and Meyer E 2011 *Rev. Sci. Instrum.* **82** 023705
- [68] Sekaric L, Carr D W, Evoy S, Parpia J M and Craighead H G 2002 *Sensors Actuators A* **101** 215–9
- [69] Azak N O, Shagam M Y, Karabacak D M, Ekinici K L, Kim D H and Jang D Y 2007 *Appl. Phys. Lett.* **91** 093112
- [70] Li M, Bhiladvala R B, Morrow T J, Siooss J A, Lew K K, Redwing J M, Keating C D and Mayer T S 2008 *Nat. Nanotechnol.* **3** 88–92
- [71] Favero I, Stapfner S, Hunger D, Paulitschke P, Reichel J, Lorenz H, Weig E M and Karrai K 2009 *Opt. Express* **17** 12813–20
- [72] Tanner S M, Gray J M, Rogers C T, Bertness K A and Sanford N A 2007 *Appl. Phys. Lett.* **91** 203117
- [73] He R, Feng X L, Roukes M L and Yang P 2008 *Nano Lett.* **8** 1756–61
- [74] Truitt P A, Hertzberg J B, Huang C C, Ekinici K L and Schwab K C 2007 *Nano Lett.* **7** 120–6
- [75] Sanii B and Ashby P D 2010 *Phys. Rev. Lett.* **104** 147203
- [76] Fu C, Deng W, Zou L, Zhu W, Wang N and Xue F 2017 arXiv:1711.04446 [cond-mat]
- [77] Weymouth A J 2017 *J. Phys. Condens. Matter* **29** 323001
- [78] Pfeiffer O, Bennewitz R, Baratoff A, Meyer E and Grütter P 2002 *Phys. Rev. B* **65** 161403
- [79] Giessibl F J, Herz M and Mannhart J 2002 *Proc. Natl Acad. Sci.* **99** 12006–10
- [80] Kawai S, Kitamura S i, Kobayashi D and Kawakatsu H 2005 *Appl. Phys. Lett.* **87** 173105
- [81] Kawai S, Sasaki N and Kawakatsu H 2009 *Phys. Rev. B* **79** 195412
- [82] Kawai S, Glatzel T, Koch S, Such B, Baratoff A and Meyer E 2010 *Phys. Rev. B* **81** 085420
- [83] Vilhena J G and Pérez R 2018 *Nat. Mater.* **17** 852
- [84] Schmid I, Marioni M A, Kappenberger P, Romer S, Parlinska-Wojtan M, Hug H J, Hellwig O, Carey M J and Fullerton E E 2010 *Phys. Rev. Lett.* **105** 197201
- [85] Degen C L, Poggio M, Mamin H J, Rettner C T and Rugar D 2009 *Proc. Natl Acad. Sci.* **106** 1313–7
- [86] Kirtley J R 2010 *Rep. Prog. Phys.* **73** 126501
- [87] Kaidatzis A and García-Martín J M 2013 *Nanotechnology* **24** 165704
- [88] Deng Z, Yenilmez E, Leu J, Hoffman J E, Straver E W J, Dai H and Moler K A 2004 *Appl. Phys. Lett.* **85** 6263–5
- [89] Phillips G N, Siekman M, Abelmann L and Lodder J C 2002 *Appl. Phys. Lett.* **81** 865–7
- [90] Lau Y M, Chee P C, Thong J T L and Ng V 2002 *J. Vac. Sci. Technol. A* **20** 1295–302
- [91] Koblishka M R, Hartmann U and Sulzbach T 2003 *Thin Solid Films* **428** 93–7
- [92] Hubmann J *et al* 2016 *Nano Lett.* **16** 900–5
- [93] Rossel C, Bauer P, Zech D, Hofer J, Willemin M and Keller H 1996 *J. Appl. Phys.* **79** 8166–73
- [94] Harris J G E, Awschalom D D, Matsukura F, Ohno H, Maranowski K D and Gossard A C 1999 *Appl. Phys. Lett.* **75** 1140–2
- [95] van Schendel P J A, Hug H J, Stiefel B, Martin S and Güntherodt H J 2000 *J. Appl. Phys.* **88** 435–45
- [96] Ciobanu L, Seeber D A and Pennington C H 2002 *J. Magn. Reson.* **158** 178–82
- [97] Poggio M and Degen C L 2010 *Nanotechnology* **21** 342001
- [98] Poggio M and Herzog B E 2018 Force-detected nuclear magnetic resonance *Micro and Nano Scale NMR* (Hoboken, NJ: Wiley-Blackwell) pp 381–420
- [99] Herzog B E, Cadeddu D, Xue F, Peddibhotla P and Poggio M 2014 *Appl. Phys. Lett.* **105** 043112
- [100] Nichol J 2014 Magnetic resonance imaging using silicon nanowire oscillators *PhD Thesis* University of Illinois at Urbana-Champaign 00000
- [101] Marcus R B, Ravi T S, Gmitter T, Chin K, Liu D, Orvis W J, Carlo D R, Hunt C E and Trujillo J 1990 *Appl. Phys. Lett.* **56** 236–8
- [102] Giessibl F J 2003 *Rev. Mod. Phys.* **75** 949–83
- [103] Poggio M, Degen C L, Mamin H J and Rugar D 2007 *Phys. Rev. Lett.* **99** 017201
- [104] Kisiel M *et al* 2015 *Phys. Rev. Lett.* **115** 046101
- [105] Volokitin A I and Persson B N J 2011 *Phys. Rev. Lett.* **106** 094502
- [106] Halbertal D *et al* 2016 *Nature* **539** 407–10
- [107] Jensen K, Kim K and Zettl A 2008 *Nat. Nanotechnol.* **3** 533–7
- [108] Malvar O, Gil-Santos E, Ruz J J, Ramos D, Pini V, Fernandez-Regulez M, Calleja M, Tamayo J and San Paulo A 2013 *Appl. Phys. Lett.* **103** 033101
- [109] Vidal-Álvarez G *et al* 2015 *Nanotechnology* **26** 145502
- [110] Cadeddu D, Munsch M, Rossi N, Gérard J M, Claudon J, Warburton R J and Poggio M 2017 *Phys. Rev. Appl.* **8** 031002
- [111] de Assis P L *et al* 2017 *Phys. Rev. Lett.* **118** 117401